博士論文

Automatic Quantitative Segmentation of Myotubes Reveals Single-cell Dynamics of S6 Kinase Activation

（**Myotube** の定量的自動セグメンテーションは

S6 キナーゼ活性化の１細胞 **dynamics** を明らかにする）

井上　晴幾

Contents

Abstract

In live cell imaging, automatic segmentation algorithm is a powerful method to quantify time series of intracellular signal activity in living cells. Automatic segmentation algorithms have thus far been developed mainly for mononuclear and round shape cells. However, a segmentation method for elongated polynuclear cells, such as differentiated C2C12 cells, has yet to be developed. By differentiation induction, C2C12 forms myotubes and undifferentiated reserve cells, making it difficult to identify background regions and correct background intensity. In this study, I developed an automatic quantitative segmentation method for myotubes using watershed segmentation of summed binary images and a two-component Gaussian mixture model. I established a C2C12 cell line stably expressing Eevee-S6K, a fluorescence resonance energy transfer (FRET) biosensor of S6 kinase (S6K). Then live cell imaging was performed to acquire time-lapse fluorescence images of the differentiated C2C12 cells. I binarized the time-lapse images and summed the binary images to enhance the contrast between myotubes and reserve cells. This enabled identification of a myotube and a myotube center. Using a myotube center instead of a nucleus, individual myotubes could be identified automatically by watershed segmentation. In addition, a two-component Gaussian mixture model which fits to fluorescence intensity histogram enabled automatic background correction without manual selection of background regions. Thus, I provide an automatic quantitative segmentation method by combining automatic myotube identification and background correction. Furthermore, S6K activities in

individual myotubes were quantified using the developed method, demonstrating that some of the temporal properties of S6K activity such as peak time and half-life of adaptation show different dose-dependent changes of insulin between cell population and individuals.

Introduction

Signaling dynamics of population and single-cell

Cells sense various extracellular stimuli and nutritional conditions and determine biological processes including cell contraction, cellular growth, differentiation and apoptosis through regulation of intracellular signaling network [1]. To understand the mechanism of these biological processes, it is important to quantify dynamics of intracellular signaling pathway. Quantification of signaling molecules has widely been characterized by (*i.e.* phosphorylation) a snapshot at a specific timepoint in a bulk assay as a cell population such as western blotting [2], [3]. However, dynamics of signaling molecules in a single cell is sometimes different from that at a cell population [4]–[8], it is necessary to quantify dynamics of signaling molecules at a single-cell level resolution.

In recent years, with the development of observation technology and computer science, intracellular signal response can be captured and analyzed at single-cell level. Along with that, it is becoming clear that single-cell dynamics has time series properties masked by cell population responses [4], [5], [7], [8]. For example, J.E. Ferrell and E. M. Machleder reported that digital response

of mitogen-activated protein kinase in individual *Xenopus laevis* oocyte and its heterogenous response generates the analogue response in the population [4]. However, such a difference in cell population and single-cells has not been clarified so far whether a general nature in intracellular signal network. As described above, to clarify the correct dynamics of the intracellular signal molecule network, it is necessary to take a live cell time series for each cell type at single cell level.

Live Cell Imaging

In single-cell studies, live cell fluorescence imaging is a powerful method to observe single-cell dynamics of signaling molecule activity [9], [10]. However, since the live cell imaging generates a large amount of time lapse images, it requires automatic segmentation algorithm to identify and quantify individual cells. Automatic segmentation algorithms have thus far been developed mainly for mononuclear and round shape cells [11]–[13]. For example, the marker based watershed segmentation is widely developed and used for efficient cell segmentation [14]–[16]. Traditional procedure of the watershed segmentation is to expand a region from a marker (*e.g.* a nucleus) as an initial flooding source until it touches the neighbors or cellular boundaries. However, since watershed segmentation requires a marker, it cannot be applied directly for polynuclear cells, such as differentiated C2C12 myotubes.

Automatic detection and quantification for elongated myotubes

C2C12 cells, derived from mice myoblasts, have been widely used to study cell differentiation and muscle functions in vitro [17]–[20]. By differentiation induction, C2C12 cells forms two kinds of subpopulations, myotubes and undifferentiated cells (called reserve cells) (Fig. 1) [21]. The elongated polynuclear form of the myotubes makes it difficult to perform automatic quantitative segmentation of individual myotubes because of the variance of fluorescence signal intensity within a myotube region. In addition, undifferentiated cells that occupy spaces between the myotubes, make it difficult to automatically identify background regions.

Insulin signaling and p70 S6 kinase

Insulin is well known as a major anabolic signal and regulates metabolism such as fat synthesis and protein synthesis in target organs such as adipose tissue, liver, and muscle via activation of the insulin signaling pathway [22]. One of the key regulators in the insulin signaling pathway is the target of rapamycin (TOR). In mammals, TOR is called mammalian TOR (mTOR) and one of the important signaling molecules highly conserved [23], [24]. mTOR forms mTOR complex 1 (mTORC1) or mTOR complex 2 (mTORC2) in the cell, and monitors the external environment. Especially, mTORC1 is known to enhance cell growth and protein synthesis by activating p70 S6 kinase (S6K) [25]. Also, it is known that constitutive activation of mTORC1 in skeletal muscle induces insulin resistance [26]. Thus, it is physiologically important to quantify the dynamics of S6K activated by mTORC1.

Purpose of this study

As described above, single-cell response and cell population response may be different. However, the difference has not been clarified so far whether a general nature in intracellular signal network. Thus, it is necessary to quantify and analyze the dynamic response in each cell type and each signaling molecule at single cell level.

In this study, I developed an automatic quantitative segmentation framework including watershed segmentation and background correction, to detect individual myotubes. Furthermore, I demonstrate some of the temporal characteristics of S6K activity such as peak time and half-life of adaptation exhibit different insulin dose dependence between cell population and individuals.

I established a C2C12 cell line that stably expressed Eevee-S6K, a fluorescence resonance energy transfer (FRET) biosensor, which monitor S6 kinase (S6K) activity [27]. Then I acquired time lapse fluorescence images both of cyan fluorescent protein (CFP) and FRET-induced yellow fluorescent protein (FRET-YFP) in differentiated C2C12 myotubes. I performed binarization of each FRET-YFP image followed by summation of the images to enhance the contrast between myotubes and reserve cells. This allowed us to detect myotube regions. In addition, to enhance contrast between myotubes and reserve cells, I converted the binary images of FRET-YFP into distance map images where all pixels have a value corresponding to the Euclidean distance to the nearest boundary pixel [28]. This

procedure resulted in selective detection of myotube regions. Furthermore, to identify individual myotubes, I detected a myotube center, rather than a nucleus, as a marker of individual myotubes. First, I converted the binary images of FRET-YFP into distance map images. Then, I performed binarization of the distance map images followed by summation of the images to enhance myotube centers. Finally, using a myotube center as a marker instead of a nucleus, individual myotubes were identified automatically by watershed segmentation.

For accurate quantification, background correction is essential. However, reserve cells that occupy the spaces between the myotubes make it difficult to identify background regions. To acquire objective measurement of signal intensity, I estimated average background intensity using two-component Gaussian mixture model (GMM) without manual selection of the background regions.

By using the automatic quantitative segmentation above, I quantified S6K activity in individual myotubes. This result demonstrated that some of the temporal characteristics of S6K activity such as peak time and half-life of adaptation show different dose-dependent changes of insulin between cell population and individuals.

Results

Automatic quantitative segmentation of differentiated C2C12 myotubes.

I developed an automatic quantitative segmentation method to identify individual myotubes from fluorescence time lapse images. The automatic quantitative segmentation method consists of two steps, Step I and II (Fig. 2). Step I is segmentation of differentiated C2C12 myotubes. In Step I, I summed the binary time-lapse images to enhance the contrast between myotubes and reserve cells. Step II is background correction. By using two-component GMM for fluorescence intensity histogram, I estimated average background intensity without manual selection of the background regions. The parameters used in each Steps were summarized in Table 1.

Step I: Segmentation of differentiated C2C12 myotubes.

In Step I, I detected myotube and myotube centers by iterating binarization including the triangle method and Otsu's method [29], [30] (Fig. 4Fig. 5), and the individual myotubes were identified by watershed segmentation using a myotube center as a marker (Fig. 6) [11]. Step I consisted of three groups that contained 11 substeps in total; Step I-i to I-iii, detection of differentiated C2C12 myotubes; Step I-iv to I-x, detection of differentiated C2C12 myotube centers; Step I-xi, Application of watershed segmentation.

Step I-i to I-iii: Detection of differentiated C2C12 myotubes. Detection of differentiated C2C12 myotubes consists of three substeps, Step I-i to I-iii (Fig. 4); Step I-i, first binarization of FRET-YFP time-lapse images; Step I-ii, summation of the first binarized images; Step I-iii, second binarization of the summed image.

In Step I-i, I pre-processed the FRET-YFP time-lapse images to reduce variation in fluorescence (See Materials and Methods) and extracted candidate regions of myotubes in each image by binarization (Step I-i first binarization in Fig. 4). For the first binarization, I applied the triangle method to the fluorescence intensity histogram of the FRET-YFP [30], because the intensity histogram was skews to the left (Fig. 4B). When using triangle method, I standardized the total area of the intensity histogram to be one prior to using the triangle method to prevent change of the threshold value due to the number of pixels. However, the binary images included not only myotube regions and also fragmented regions of reserve cells. To extract only myotube regions, enhancement of the contrast between myotubes and reserve cells will be needed.

In Step I-ii, I summed the binary images (Step I-ii Summation in Fig. 4A). By the summation, the contrast between myotubes and reserve cells were enhanced because the myotubes were thicker and brighter than reserve cells.

In Step I-iii, I extracted myotube regions by binarizing the summed binary images. (Step I-iii Second binarization in Fig. 4A). The threshold of the second binarization was determined using the

Otsu's method because the intensity histogram of the summed image was bimodal (Fig. 4C). Otsu's method is a statistical thresholding method to find a threshold that minimizes the within-class variance [29]. Thus, I detected myotubes by iterating binarization including the triangle method and Otsu's method, using the summed binary image of FRET-YFP time-lapse images (Fig. 4D). However, some of the myotubes were identified as one continuous region rather than as individual myotubes. Additional segmentation is required to identify individual myotubes.

Step I-iv to I-x: Detection of differentiated C2C12 myotube centers. In fluorescence imaging, watershed segmentation has been widely used to identify individual cells [11]. However, since watershed segmentation using a nucleus as a marker, polynuclear and elongated shape cells such as myotubes could not be identified so far. Therefore, I extracted a myotube center, instead of a nucleus, as a marker for watershed segmentation.

Detection of differentiated C2C12 myotube centers consists of seven substeps, Step I-iv to I-x (Fig. 5A); Step I-iv, first binarization of FRET YFP time lapse images; Step I-v, transformation from the first binary images into distance map images; Step I-vi, second binarization of the distance map images; Step I-vii, summation of the second binary images; Step I-viii, thrird binarization of the summed images; Step I-ix, labeling of the third binary image; Step I-x, denoising of the labeled image.

In Step I-iv, I binarized smoothed images by triangle method for extracting candidate regions of

myotubes.

In Step I-v, I transformed the binary images into distance map images to emphasize myotube centers (Step I-v Distance transform in Fig. 5A). However, some regions in the center of myotube were not emphasized by the presence of nuclei. This leads over-segmentation of the regions of myotube center.

In Step I-vi, to extract candidate regions of myotube center, I binarized the distance map images by triangle method (Step I-vi Second binarization in Fig. 5A). Then I summed the binarized images to enhance the contrast between myotube centers and the other regions (Step I-vii Summation in Fig. 5A). Because a nucleus moved frequently within a myotube, the summation of the binarized images attenuated the influence of nuclear existence.

In Step I-viii, to extract regions of myotube center, I binarized the summation of the binarized images by Otsu's method (Step I-viii Third binarization in Fig. 5A).

In Step I-ix, I labeled the third binary image with one continuous region as one myotube center (Step I-ix Labeling in Fig. 5A). Although the labeled image appeared to be successful in detecting myotube centers, it contained lots of small debris ranging from one to dozens of pixels in length (Figs. Fig. 5B, C). This leads over-segmentation of individual myotubes when using a region of myotube center as a marker for watershed segmentation.

In Step I-x, therefore, I performed skeletonization of the labeled image, then removed the debris

by the short length. Skeletonization is a thinning algorithm that removes outer pixels of a region to find its medial axis and a length was defined as a number of pixels of a skeletonized region. Since the length histogram of the myotube centers was skewed to the left, the threshold of the length was determined using triangle method for the histogram (Fig. 5C). Thus I identified individual regions of myotube center by removing the regions smaller than the threshold (Step I-x Denoising in Fig. 5A, Table 1).

Throughout the first ten substeps (Step I-i to I-x), I obtained an individual myotube region as a boundary for watershed segmentation, and an individual myotube center as a marker for watershed segmentation. This allowed me to identify regions of individual myotube by watershed segmentation using a region of myotube center as a marker.

Step I-xi: Application of watershed segmentation. In Step I-xi, using the individual regions of myotube center in Step I-x as the markers, watershed segmentation was applied to the myotube regions identified in Step I-iii. The regions of individual myotube were identified by removing the regions smaller than a threshold (Fig. 6).

Performance of segmentation.

In this study, the use of iterative binarization including the triangle method and Otsu's method enabled

me to develop an automatic segmentation method of individual myotubes. However, the changes of excitation intensity and number of time-lapse images could affect the segmentation performance because the thresholding methods including triangle method and Otsu's method are based on the intensity histogram of an image. Therefore, to test the segmentation performance, I manually selected ground truth of myotube regions from the MIP image as the reference for the test (Fig. 7). Then I compared the segmentation performance of the developed method with other conventional segmentation methods (Otsu's method and triangle method) by fluctuating excitation light transmittance and the number of time-lapse images (Fig. 8).

The segmentation performance was evaluated based on Jaccard index [31] calculated between the ground truth and the regions identified by each method. The Jaccard index is an indicator of the similarity between two regions [11], and defined as

$$\text{Jaccard index} = \frac{X \cap Y}{X \cup Y}, \tag{1}$$

where X and Y are the regions of interest. The higher value of the index, the more similarity. Note that, like the ground truth, identification of the myotube regions by triangle method and Otsu's method used the MIP image. It was an advantageous performance comparison to Otsu method and triangle method. Also note that it is difficult to manually select perfect regions of myotubes because the boundaries of myotube are ambiguous.

With 12 % or less transmittance of excitation light, Jaccard index of developed method was

significantly higher than the conventional methods. (Fig. 8A). This result indicates that our method is more robust to change in excitation intensity than the conventional segmentation methods. For reduction of number of images, there is no significant difference under every condition (Fig. 8B). These results suggest that the segmentation performance of developed method is comparable to the conventional methods, in the change of the number of images. In addition, developed method has an advantage that adjacent myotubes can be identified individually by implementing detection of myotube center as a marker for watershed segmentation.

Step II: Background correction.

The various factors, such as the setup of the optical system, properties of the detector, and the fluorescent probe, often make the background intensity non-uniform even in a same field.

Furthermore, in live cell fluorescence imaging, researchers often perform the imaging with weak excitation light to prevent photo-bleaching and photo-toxicity of the cells. However, this generates as image with a low signal-to-noise ratio. In ratiometric data, such as the FRET ratio, failure to identify of background regions causes serious artifacts when quantifying signal intensity. Therefore, the proper background correction is required [32].

The method manual selection of background regions near the regions of interest followed by subtraction of the intensity has been widely used for background correction [18], [33], [34]. However,

in the case of differentiated C2C12 cells, existence of reserve cells between myotubes makes it difficult to identify background regions (Fig. 1). Therefore, to avoid the selection of background region, a two-component Gaussian mixture model (GMM) which fits to a fluorescence intensity histogram was used for background correction.

Background correction consisted of five substeps (Fig. 9); Step II-i, maximum intensity projection (MIP) of smoothed FRET-YFP time-lapse images, Step II-ii, binarization of the MIP image; Step II-iii, NOT AND (NAND) operation on the raw time lapse fluorescence images and binary MIP image; Step II-iv, estimation of background intensity using two-component Gaussian mixture model (GMM). Step II-v, signal intensity quantification of individual myotubes.

In Step II-i, I performed MIP to keep only the pixels of maximum intensity along the z-axis of stacked images. The MIP can emphasize the pixels where the myotubes existed through the time series (Step II-i in Fig. 9).

In Step II-ii, binarization of the MIP images enabled reliable separation of the pixels where the myotubes existed through the time series from other pixels including reserve cells and background regions (Step II-ii in Fig. 9).

In Step II-iii, to extract a region composed of reserve cells and background regions, I performed the NAND operation on the raw time-lapse fluorescence images and the binary MIP image (Step II-iii in Fig. 9).

In Step II-iv, since the regions of except for myotubes consists of reserve cells and background, I used the two-component GMM to estimate intensity distributions of background in CFP and FRET-YFP time-lapse images, respectively (Step II-iv in Fig. 9). In the two-component GMM, the histogram was divided into two components of Gaussian distributions which corresponded to intensity distribution of a region that included reserve cells and background regions. The background intensity was estimated as an average of the lower component.

In Step II-v, signal intensities of CFP and FRET-YFP in individual myotubes were quantified after subtraction of the estimated background intensity from each time-lapse image. Then I calculated a time series of the FRET ratio (FRET-YFP/CFP) (Step II-v in Fig. 9).

Performance of background correction.

For evaluating performance of the background correction, I compared the performance of background correction using two-component GMM with other histogram-based background correction methods using raw histogram (RAW) and kernel density estimation (KDE) (Fig. 10). In a background correction using RAW, background intensity was estimated as the mode intensity of the histogram. In background correction using KDE, background intensity was estimated as the mode intensity of the histogram, approximated by kernel density estimation.

In the all background corrections using RAW, KDE and two-component GMM, Steps II-i to II-iii

are common steps. In Step II-iv, I estimated the background intensities using RAW, KDE and two-component GMM, respectively. In Step II-v, By using each method for estimation and correction of background intensity, the signal intensities of CFP and FRET-YFP in individual myotubes were quantified and calculated time series of the FRET ratio (FRET-YFP/CFP) (Fig. 10A, upper panel).

As the performance of the background correction, I calculated an area under the curve (*AUC*) of the absolute first-order difference of the time series of FRET ratio. The *AUC* is described by

$$d_i = |y_i - y_{i-1}|, \tag{2}$$

$$AUC = \sum_{i=1}^{N-1} \frac{\Delta t}{2}(d_i + d_{i+1}), \tag{3}$$

Where $\{y_1, y_2, \ldots, y_N\}$ is the time series of the FRET ratio at a frame index *i, N* is the total number of frames, $\{d_1, d_2, \ldots, d_{N-1}\}$ is the absolute difference between y_i and y_{i-1}, Δt is the time interval between frames (Fig. 10A, lower panel).

The median of the *AUC* when using two-component GMM was significantly smaller than those using RAW or KDE (Fig. 10B). This indicates that the two-component GMM has the best performance among the three methods. Furthermore, when using two-component GMM, the estimated distributions are continuous and the parameters including the mean and the variance are automatically determined. These are advantages not in RAW and KDE.

I compared the performance of background correction using two-component GMM with other background correction methods using semi-automatic two-component GMM and manual estimation.

(Fig. 7Fig. 11). In the semi-automatic two-component GMM and manual estimation, I generated the MIP image from FRET-YFP time-lapse images, then manually selected ground truth of the myotubes (Fig. 7). Especially in the semi-automatic two-component GMM, the background intensity was estimated using two-component GMM that fits to an intensity histogram of the regions except for the ground truth of the myotubes. In the manual estimation, the background intensity was estimated as an average intensity of manually selected three regions. By using each background correction method, I quantified signal intensities of CFP and FRET-YFP and calculated a time series of the FRET ratio (Fig. 11A). Then, I calculated the *AUC* in eq. (3) for evaluating the performance of background correction.

There was no significant difference in median of the *AUC*s among the three background correction methods. This indicates that the performance of background correction using two-component GMM is comparable to the manual estimation (Fig. 11B). Furthermore, the two-component GMM has an advantage to provide objective quantification.

In an intramolecular FRET biosensor such as Eevee-S6K, fluorescent molecules of CFP and YFP are linked by a linker domain, and a total variation of the time series of CFP and FRET-YFP should show a high correlation in a steady state. Therefore, I calculated the coefficients of determination of the *AUCs* in eq. (3) between CFP and FRET-YFP when using each background correction method including RAW, KDE, Manual, Semi-automatic two-component GMM and two-component GMM (Fig. 12). The background correction using two-component GMM shows the highest coefficient of

determination of the *AUC*s, indicating that the background correction using two-component GMM is the most reasonable method for background correction among them.

Furthermore, I conformed whether the developed method using two-component GMM can be used for myotubes under other conditions, such as myotubes stimulated with insulin or myotubes expressing an ATP probe stimulated with an electrical pulse stimulation (Fig. 13A and B). To confirm the availability under other conditions, first I chose the pairs of myotube regions where the Jaccard index between manual selection and the identification by the developed method was larger than 0.5. Then I calculated a correlation coefficient of the time series of FRET ratio in each pair. In insulin stimulation for differentiated C2C12 cells stably expressing Eevee-S6K, most of the correlation coefficients were larger than 0.98, indicating that the developed method is comparable to the manual estimation (Fig. 13C, upper panel). In electrical pulse stimulation for differentiated C2C12 cells stably expressing mitAT1.03, which is FRET biosensor for monitoring ATP concentration in a mitochondrion [35], all the correlation coefficients were larger than 0.98 (Fig. 13C, lower panel), indicating that developed method is comparable to the manual estimation.

The different characteristics between cell population and individuals in C2C12 myotubes.

The developed method aims to acquire time series of fluorescent intensity in individual myotubes from fluorescence time-lapse images. Using the developed method, I tried to quantify insulin-dependent

S6K activation and looked for different characteristics between cell population and individual myotube.

From the obtained fluorescence time lapse images, I quantified time series of S6K activity in individual myotubes stimulated with various dose of insulin (0 nM to 100 nM) (Fig. 14A). Then I quantified the characteristics such as Peak, Peak time, AUC, etc., from the time series (Fig. 14A lower right panel, B). In the cell population, Peak, AUC, Half-life of adaptation and Intensity at half-life of adaptation increased dose-dependently of insulin. Variance in Peak time decreased, and Adaptation precision slightly decreased dose-dependently of insulin.

The correlation analysis of characteristics in between bootstrap subset (Bootstrap) as the cell population and all data (All) as the individuals was performed to investigate the difference between the cell population and the individuals (Fig. 15). The correlation of Peak time with all other characteristics were significantly different between the cell population and the individuals. The reason why the Peak time was significantly different in the combinations with all characteristics may be because the variance of Peak time decreased dose-dependently of insulin (Fig. 14B). Consistent with this, the correlations between Peak time with all other properties were decreased in a dose-dependent manner of insulin (Fig. 16). Also, the correlation of Half-life of adaptation with all other properties were significantly different between the cell population and the individuals. This indicates that Half-life of adaptation shows different responses between the cell population and individuals. In Half-life

of adaptation, differences in the characteristics except for Peak time between the cell population and individuals can be classified into three groups that show higher correlation in the cell population than the individuals, higher correlation in the individuals than the cell population, and reversed relationship between the cell population and individuals (Fig. 15).

In the combinations with Half-life of adaptation, Peak and AUC showed stronger correlation in the cell population than in the individuals (Fig. 15A, B). Consistent with this, the distributions of Peak and AUC were more separated in the cell population than the individuals (Fig. 17A). Adaptation precision showed higher correlation with Half-life of adaptation in the individuals than in the cell population (Fig. 15A, B). Furthermore, in the individuals, the correlation of Half-life of adaptation with Adaptation precision in each dose decreased dose-dependently of insulin (Fig. 16 bottom center, Fig. 17B). This indicates that the combination of Half-life of adaptation and Adaptation precision in individuals conserves characteristic response not found in the cell population. In the combination of Intensity at half-life of adaptation and Half-life of adaptation, the correlation in the cell population was positive, whereas in the individuals was negative (Fig. 15A, B). The distribution of Half-life of adaptation and Intensity at half-life of adaptation for each dose varied in the negative correlation direction in individuals, but not in the cell population (Fig. 17C). Furthermore, the correlations between Half-life of adaptation and intensity at Half-life of adaptation in each dose of insulin were negative in the individuals (Fig. 16 bottom right). These results indicate that the individuals possess

hidden characteristics that can not be seen in the cell population. Thus, some of the characteristics of insulin dose-dependent S6K activation differ between the cell population and the individuals.

Materials and methods

Cell Culture

C2C12 cells (kindly provided by Takeaki Ozawa, University of Tokyo, Tokyo, Japan) were cultured at 37°C under 5% CO_2 in Dulbecco's modified Eagle's medium (DMEM), (High Glucose) with L-Glutamine and Phenol Red (Wako Pure Chemical Industries Limited, Osaka, Japan) supplemented with 10% fetal bovine serum (Nichirei Bioscience Incorporated, Japan). For differentiation induction, C2C12 cells were seeded on 35 mm/Collagen Coated Dish Collagen type I (IWAKI, Japan) at a concentration of 1.0×10^5 cells/dish and cultured for two days under conditions described above until confluent, and then confluent cells were cultured in DMEM with L-Glutamine and Phenol Red supplemented with 2% horse serum (Nichirei Bioscience Incorporated) for seven days [36].

Construction of C2C12 cell line stably expressing FRET biosensors.

C2C12 cells stably expressing FRET biosensors, Eevee-S6K (plasmid was kindly provided by Kazuhiro Aoki, National Institute for Basic Biology, Aichi, Japan) [27], [37] and mitAT1.03 (plasmid was kindly provided by Hiromi Imamura, Kyoto University, Kyoto, Japan) [35], were constructed using the PiggyBac Transposase System (System Biosciences, U.S.A.), respectively. Three hundred μL of Opti-MEM (Life technologies, U.S.A.), 4 μL of Lipofectamin 2000 (Invitrogen, U.S.A.), 1.0 μg of PiggyBac transposon vector clone (kindly provided by Kazuhiro Aoki, National Institute for Basic

Biology, Aichi, Japan) and 0.2 μg of PiggyBac transposase expression vector (PB210PA-1, Funakoshi, Japan) were mixed and let stand for 5 min. Thereafter, 70% confluent C2C12 cells were plated on a 35 mm dish and transfected with the mixture and incubated for 6 h. For selection of infected cells, the cells were cultured with DMEM (High glucose) with L-Glutamine and Phenol Red containing 10% fetal bovine serum and 20 μg/mL of Blasticidin S Hydrochloride (Wako, Japan). Selected cells were seeded on a Cell Culture Dish 430167 (Corning Incorporated, U.S.A.) and cultured until forming the colonies. The colonies were picked and seeded on a Cell Culture Dish 430167. After seeding and proliferation, the cells were stored at a concentration of 1.0×10^5 cells/mL with Bambanker (NIPPON Genetics, Japan). Eevee-S6K is localized in the cytosol and mitAT1.03 is localized in the mitochondria.

Live-cell imaging.

C2C12 myotubes were starved in 2 mL of Medium199, Hanks' Balanced Salts (Life technologies, U.S.A.) overnight and then mineral oil (Sigma Aldrich) was stratified to prevent vaporization of the medium prior to the fluorescence time-lapse imaging. Fluorescence time-lapse imaging was performed with an inverted fluorescence microscope, IX 83 (Olympus, Tokyo, Japan) equipped with a UPLSAPO10X2 objective lens (Olympus), a ORCA-R2 C10600-10B CCD camera (Hamamatsu Photonics), a U-HGLGPS mercury lamp (Molecular Devices, Sunnyvale, CA), XF3075 and XF3079 emission filter for CFP and YFP (Omega Optical), respectively, and an MD-XY30100T-META

automatically programmable XY stage (Molecular Devices).

All the images of myotubes were 1344×1024 pixels and 0.645 μm/pixel. Time-lapse images of myotubes expressing Eevee-S6K were acquired for 650 min every 5 min (total 131 frames) with eight stage positions. Time-lapse images of myotubes expressing mitAT1.03 were acquired for 45 min every 1 min (total 46 frames) with one stage position. After background subtraction, FRET-YFP/CFP ratio images were created with Meta-Morph software (Universal Imaging, West Chester, PA).

Pre-processing of images.

A myotube region in an obtained fluorescence image shows a non-uniform distribution of fluorescence because of its polynuclear and elongated form. For proper identification of myotube regions, smoothing of obtained images is essential. I first applied a median filter to remove outliers [38] followed by white top-hat filter to reduce variation of fluorescence intensity (Fig. 3).

Image analysis.

Our proposed method was developed using Python and Python modules, including Mahotas [39], Scikit-image [40] and Scikit-learn [41] for automatic quantification. Fiji [42] was used for manual quantification of fluorescence intensity of FRET-YFP and CFP. The FRET-YFP and CFP intensities were averaged over the whole myotube area.

Significance test of the difference between two correlation coefficients.

Fisher's z-transformation of correlation coefficients r is given by

$$z_i = \frac{1}{2}\ln\frac{1+r_i}{1-r_i}, i \in \{1,2\}, \qquad (3)$$

where i is an index of correlation coefficient. A z score of the difference between two correlation coefficients, described by

$$z = \frac{z_1 - z_2}{\sqrt{\frac{1}{n_1 - 3} + \frac{1}{n_2 - 3}}}, \qquad (4)$$

where n_1 and n_2 are numbers of data corresponding to r_1 and r_2. As the z score follows normal distribution, significance test was performed with significance level $\alpha = 10^{-3}, 10^{-5}, 10^{-7}$.

Discussions

Advantages of the developed segmentation method.

In previous research, many cellular segmentation algorithms have been developed for mononuclear and round shape cells [11], [12], [43]. However, methods for automatic segmentation of elongated polynuclear cells, such as differentiated C2C12 cells, has not yet been developed. Indeed, intracellular signal activity and reactive oxygen species in myotubes have been measured only by manual selection of myotube regions [18], [33], [34]. Since the developed method can be used in unsupervised, it can be used for any type of polynuclear and deformed cells. However, it is difficult to apply the developed

method to moving cells because cell tracking does not include in the developed method. Using our method for images every fixed period and implementing cell tracking, there is a possibility that our method can be applied to moving cells. Since the developed method uses time-lapse images to enhance contrast between the background and the objects, the segmentation may fail if the number of images is insufficient.

Using deep learning, some recent studies achieved improvements of accuracy and throughput of segmentation of cells [44]. Deep learning is a powerful tool for cellular segmentation of the complex region with high accuracy and high throughput and may be used effectively for elongated polynulcear cells, such as C2C12 myotubes. While the deep learning has wide range of availability, it requires a large amount of training data and computational resources in general. Therefore, a segmentation result by deep learning depends on the training data. Especially, in cells with ambiguous cell boundaries such as myotubes, there is possibility to learn bias of manual selection of the myotube regions. On the other hand, developed method does not require any training data and few computational resources.

The calculation time of the developed method was less than 15 min even when processing 131 images including from segmentation to quantification, using AMD Ryzen 7 1800X (Table 2). When only performing the segmentation, the developed method took about 30 sec for one dataset (131 frames). This is fast enough compared with manual segmentation which took about 15-20 min using ROI tool in Fiji. In background correction, two-component GMM took about 3 sec per image. Since

the developed method was fully automated after setting the parameters for the segmentation (Table 1), the consuming time of two-component GMM is practical time. This is practical time, because our method was fully automated after setting the segmentation parameters.

Heterogeneity of cell response.

I quantified S6K response for insulin stimulation in individual myotubes and demonstrated that the individuals possess hidden characteristics that can not be seen in the cell population. This raises the possibility that some of the characteristics may be underestimated or incorrectly estimated by the cell population analysis. Therefore, single-cell analysis is important to reveal hidden characteristics of the cell system that can not be observed in the cell population. In addition, single-cell analysis will address whether variation of cell population is derived from intra-cellular variation or inter-cellular variation. For instance, to quantify information transmission of intracellular signaling within these variations, the information theory is needed to handle a distribution of cellular response as an information [45]–[49].

Signal transduction in skeletal muscle has thus far been studied by conventional bulk assays such as western blot, that reflect the activity at cell population level [50]–[54]. In contrast, the developed method can automatically identify and quantify signal activity of single myotube, and will open the door to single-cell analysis in signal transduction of skeletal muscle.

Figures and tables

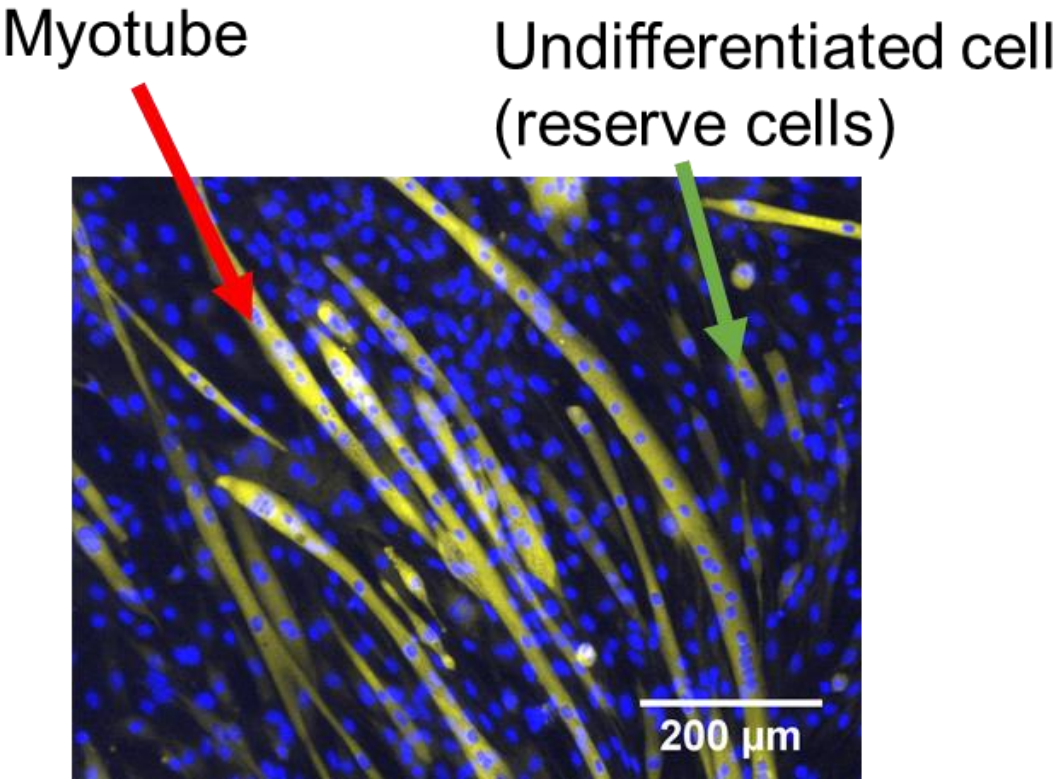

Fig. 1 Differentiated C2C12 myotubes stably expressing Eevee-S6K. Differentiated C2C12 cells stably expressing Eevee-S6K (Yellow). Nuclei were stained with DAPI (Blue). Because myotubes are much thicker than reserved cells, myotubes (red arrows) were much brighter than reserve cells (green arrows). Because of the relatively weaker fluorescence signal in reserve cells, only nuclear signals, but not cell body signals, were visible.

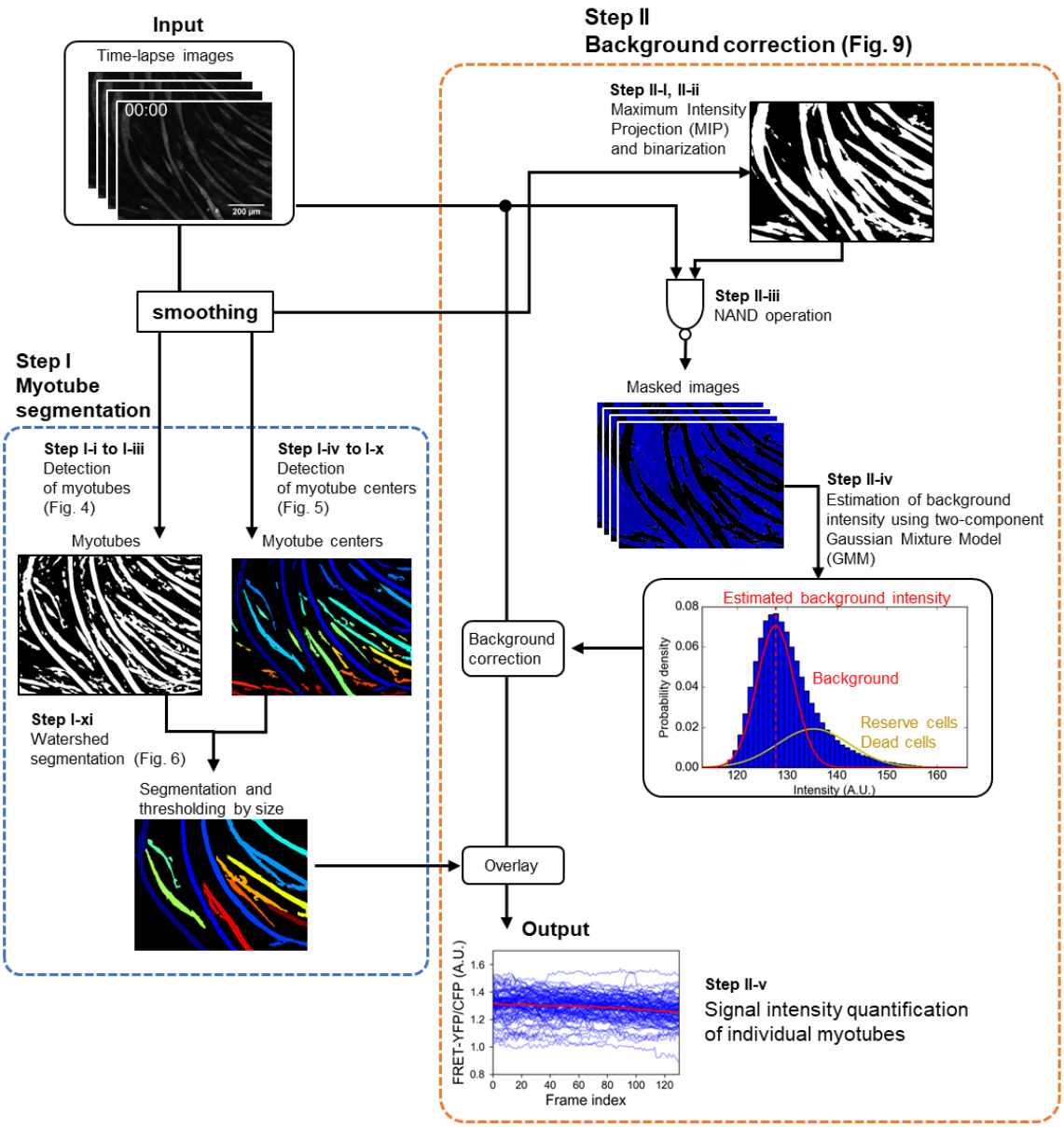

Fig. 2 Procedures of the automatic quantitative segmentation of myotubes using time-lapse images. The automatic quantitative segmentation method consists of two steps, Step I and II; Step I, myotube segmentation; Step II, background correction.

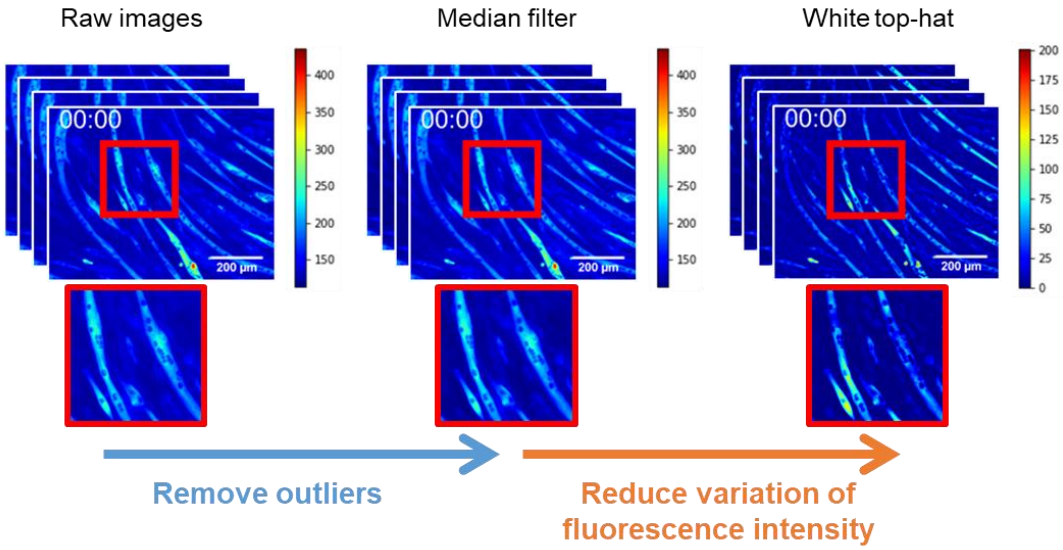

Fig. 3 Pre-processing of fluorescence images. I applied median filter with $\mathbf{5 \times 5}$ square window to the raw FRET-YFP time-lapse images. Then, I applied white top-hat to images processed by the median filter. Filter window of the white top-hat is $\mathbf{35 \times 35}$ and $\mathbf{30 \times 30}$ in identification of myotubes and identification of myotube centers, respectively.

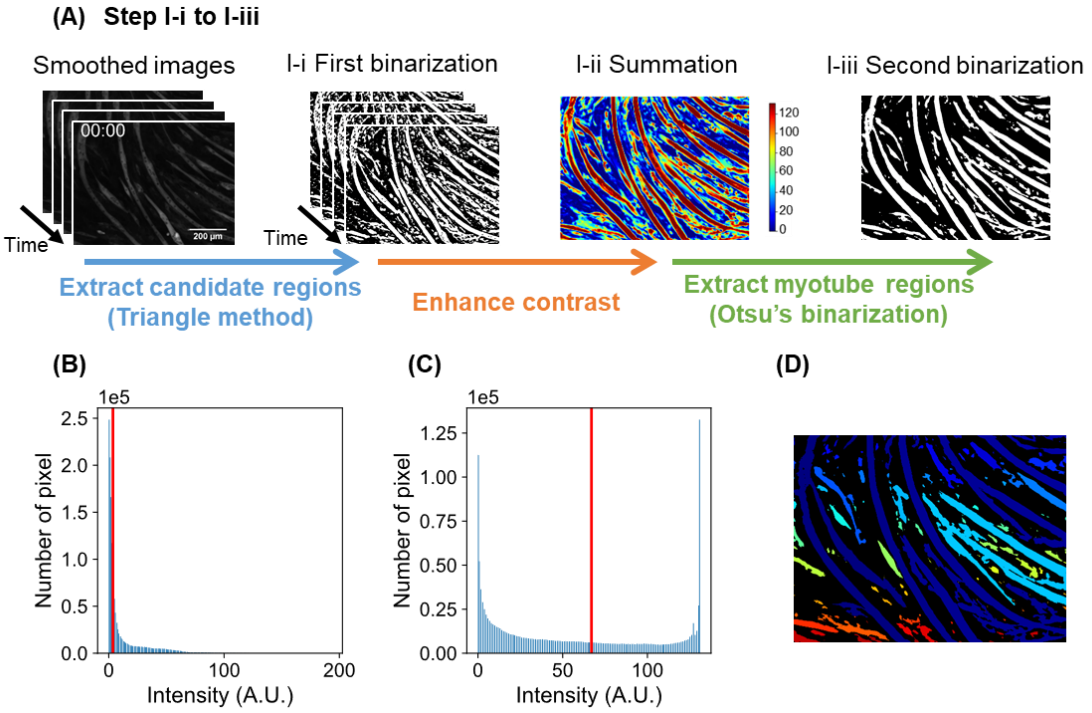

Fig. 4 Detection of differentiated C2C12 myotubes. (A) Detection of myotubes consisted of three substeps; Step I-i, first binarization; Step I-ii, summation; Step I-iii, second binarization. In step I-ii, the intensity increases from blue to red. (B) FRET-YFP intensity histogram at frame 0. Red line indicates the threshold value, which was determined by the triangle method. (C) Intensity histogram of the summed binary image. The red line indicates the threshold value, as determined by Otsu's method. (D) Labeled images of detected myotubes. One color corresponds to one continuous myotube region. Black denotes a region of either reserve cells or background.

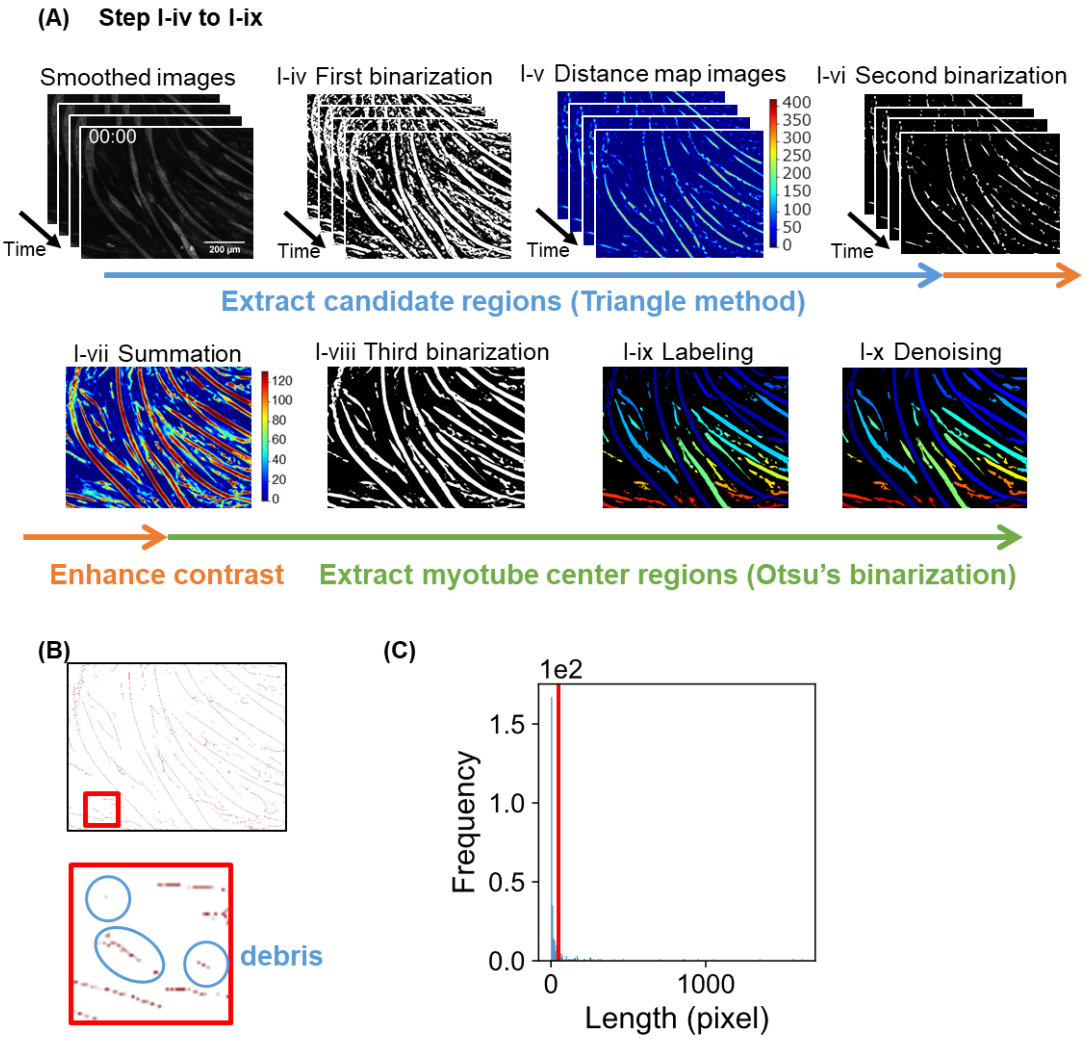

Fig. 5 Detection of myotube centers. (A) Detection of myotube centers consists of seven substeps; Step I-iv, first binarization of fluorescence time-lapse images; Step I-v, transformation of the first binary images into distance map images; Step I-vi, second binarization of the distance map images; Step I-vii, Summation of the second binary images; Step I-viii, third binarization of the summed images; Step I-ix, labeling of the third binary image; Step I-x, denoising of the labeled image. Note that in Step I-v and I-vii, colors denote intensity in a pixel, whereas, in Step I-ix and I-x, one color corresponds to one continuous region. Black indicates either reserve cells or background regions. (B)

Skeletonized image of a labeled image. (C) Length histogram of a skeletonized image. We assumed that length is a number of pixels in a continuous region of a skeletonized image. The red line indicates threshold length determined by the triangle method.

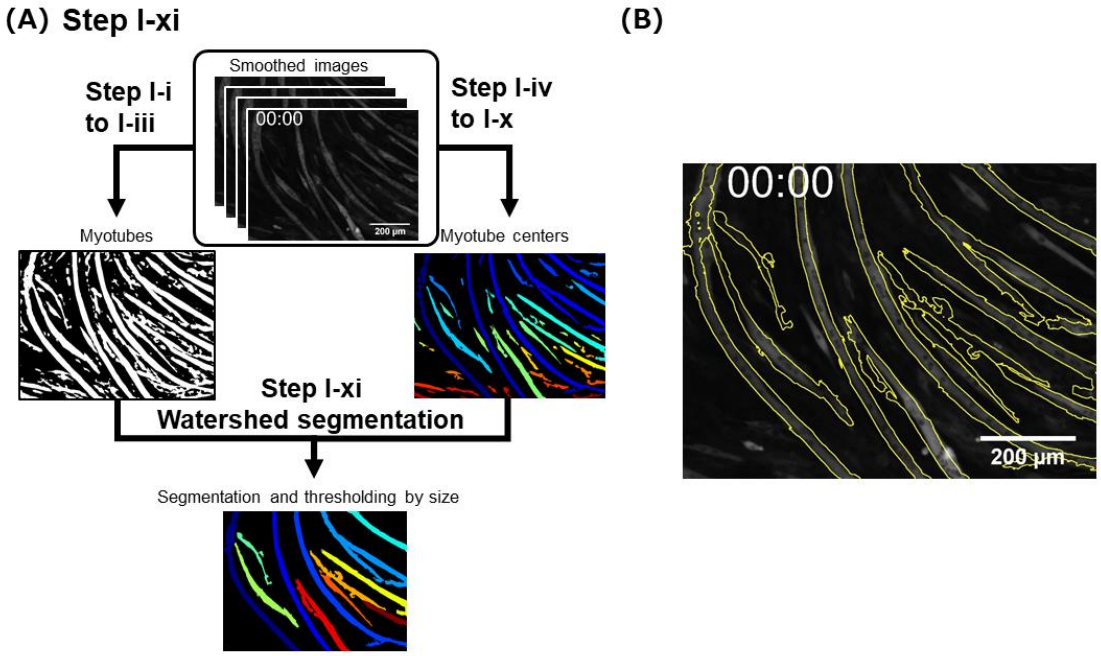

Fig. 6 Watershed segmentation. (A) Myotubes and myotube centers were identified from time-lapse FRET-YFP images. An identified myotube was used as a boundary for watershed segmentation. An identified myotube center was used as a marker for watershed segmentation. Watershed segmentation was performed using identified myotubes and myotube centers, areas that were less than 10000 were removed. (B) Overlays of raw FRET-YFP time-lapse image at frame 0 and the result of watershed segmentation. Yellow lines indicate contours of segmented myotube regions.

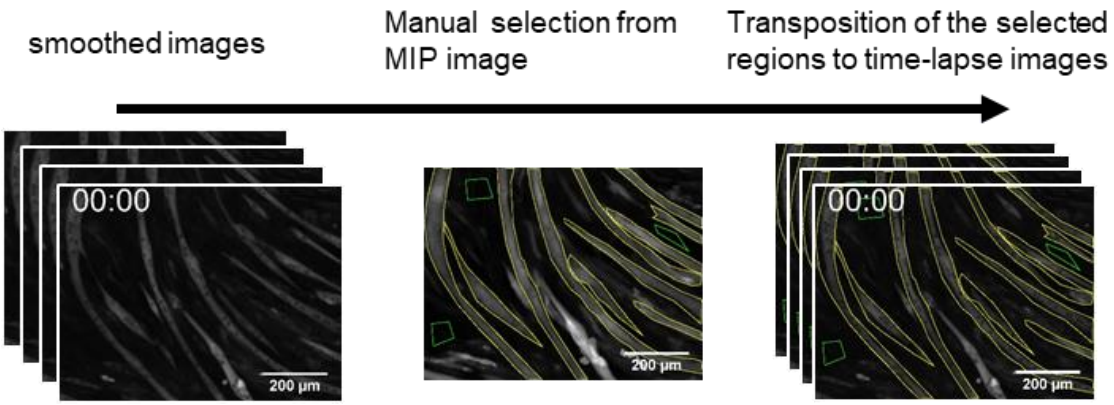

Fig. 7 Manual selection of myotube regions. I generated MIP images from the pre-processed FRET-YFP time-lapse images and manually selected the myotube regions and background regions, respectively. The yellow line indicates myotube regions. The green line indicates background regions. I transposed the regions to raw time-lapse images of CFP and FRET-YFP and quantified intensities of CFP and FRET-YFP in each region. Three background regions were selected, and the average of the intensities was used as background intensity.

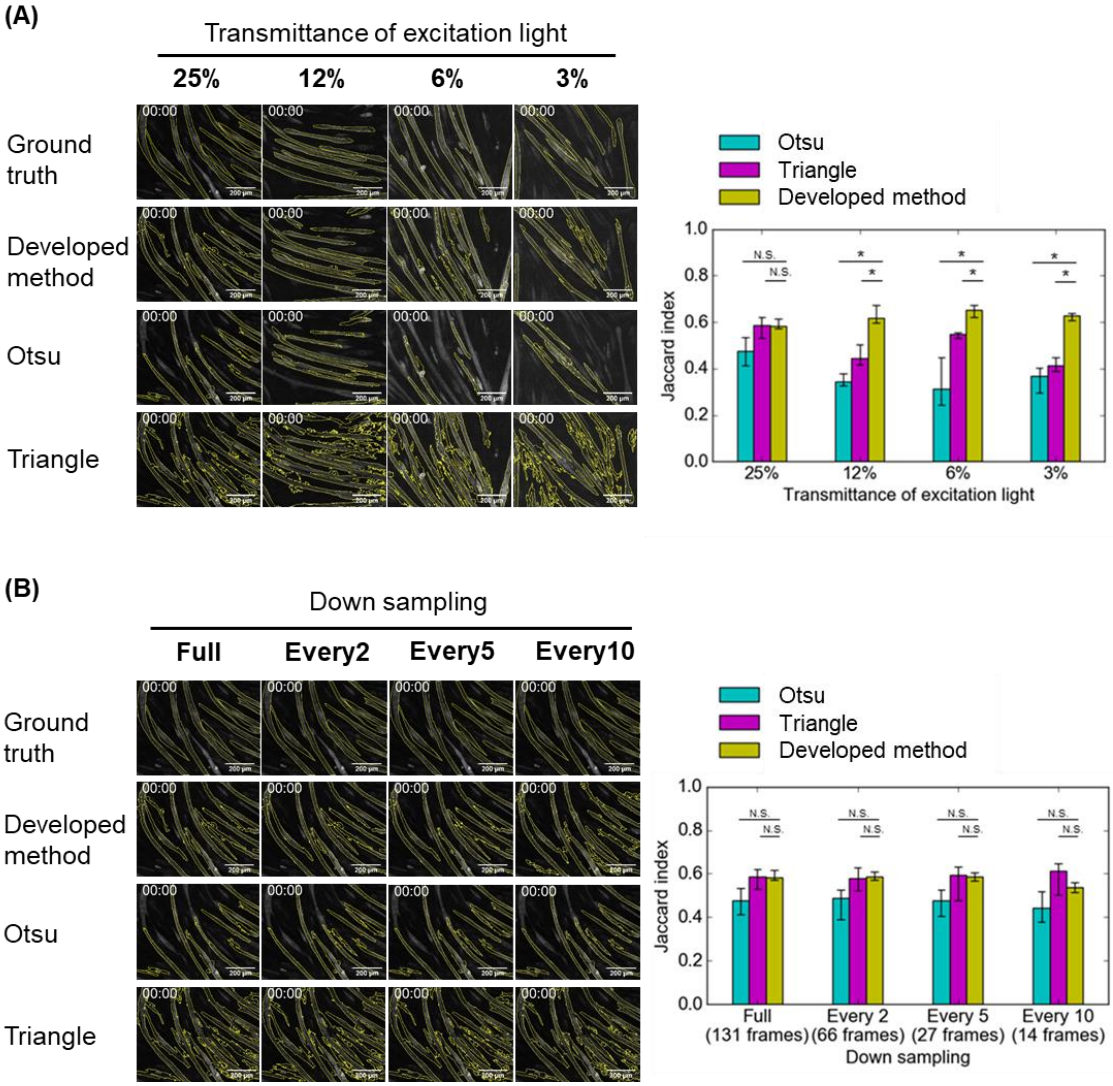

Fig. 8 Accuracy of segmentation. (A) Left panel: Representative segmentation results with the indicated transmittance of excitation light (25%, 12%, 6% and 3%). Yellow lines are contours of individual myotubes. Right panel: Jaccard indices in each transmittance of excitation light (median ± iqr, n = 8 stage positions). Segmentation result of ground truth was used as the reference to calculate the Jaccard index. N. S. (Not significant), $p > 0.05$ (Welch's t-test). p values were corrected by Bonferroni correction. (B) Representative segmentation results when changing the number of time-lapse images by resampling every two to ten images. Full shows segmentation results using the full

set of the images. Every 2, Every 5 and Every 10 indicate segmentation results obtained by resampling the images at every two, five and ten time points, respectively. Transmittance was set to 25%. Right panel: Jaccard indices in each number of time-lapse images (median ± iqr, n = 8 stage positions).

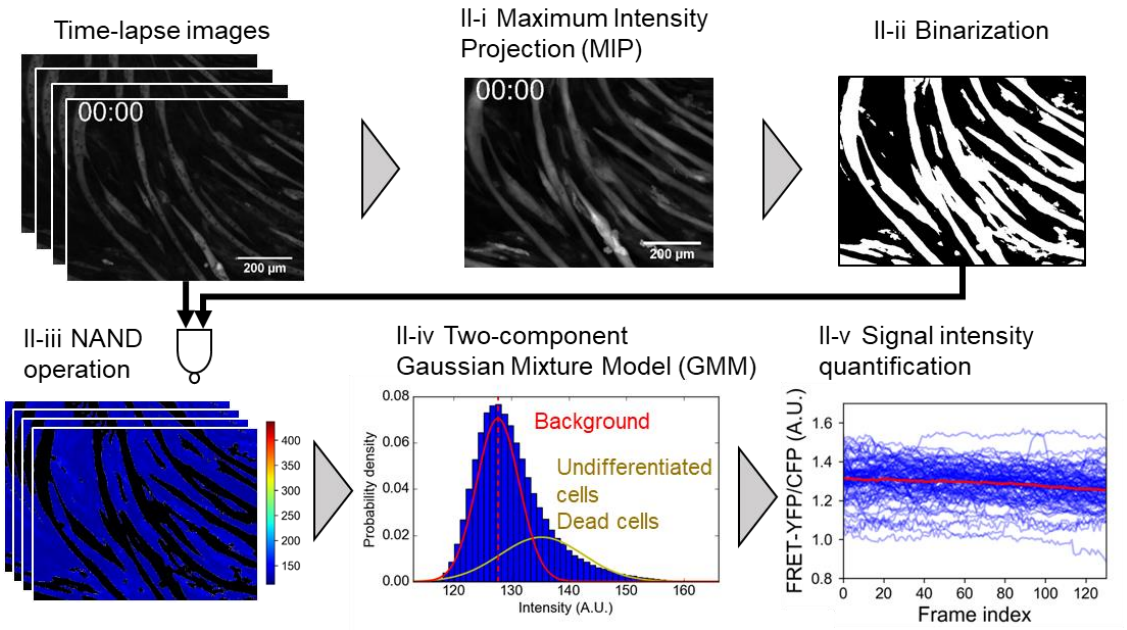

Fig. 9 Background correction. Background correction consists of five substeps; Step II-i, maximum intensity projection (MIP); Step II-ii, binarization of the MIP image; Step II-iii, NOT AND (NAND) operation; Step II-iv, two-component Gaussian mixture model (GMM). Step II-v, signal intensity quantification. In Step II-iii, the intensity increases from blue to red. In Step II-iv, a red line indicates estimated background intensity distribution and a red dashed line indicates an average of the distribution as the estimated background intensity. A yellow line indicates the estimated intensity distribution of a region that included reserve cells and dead cells. In Step II-v, each blue line corresponds to the time series of each individual myotube. A red line indicates the average time series of the FRET ratio of myotubes in each background correction.

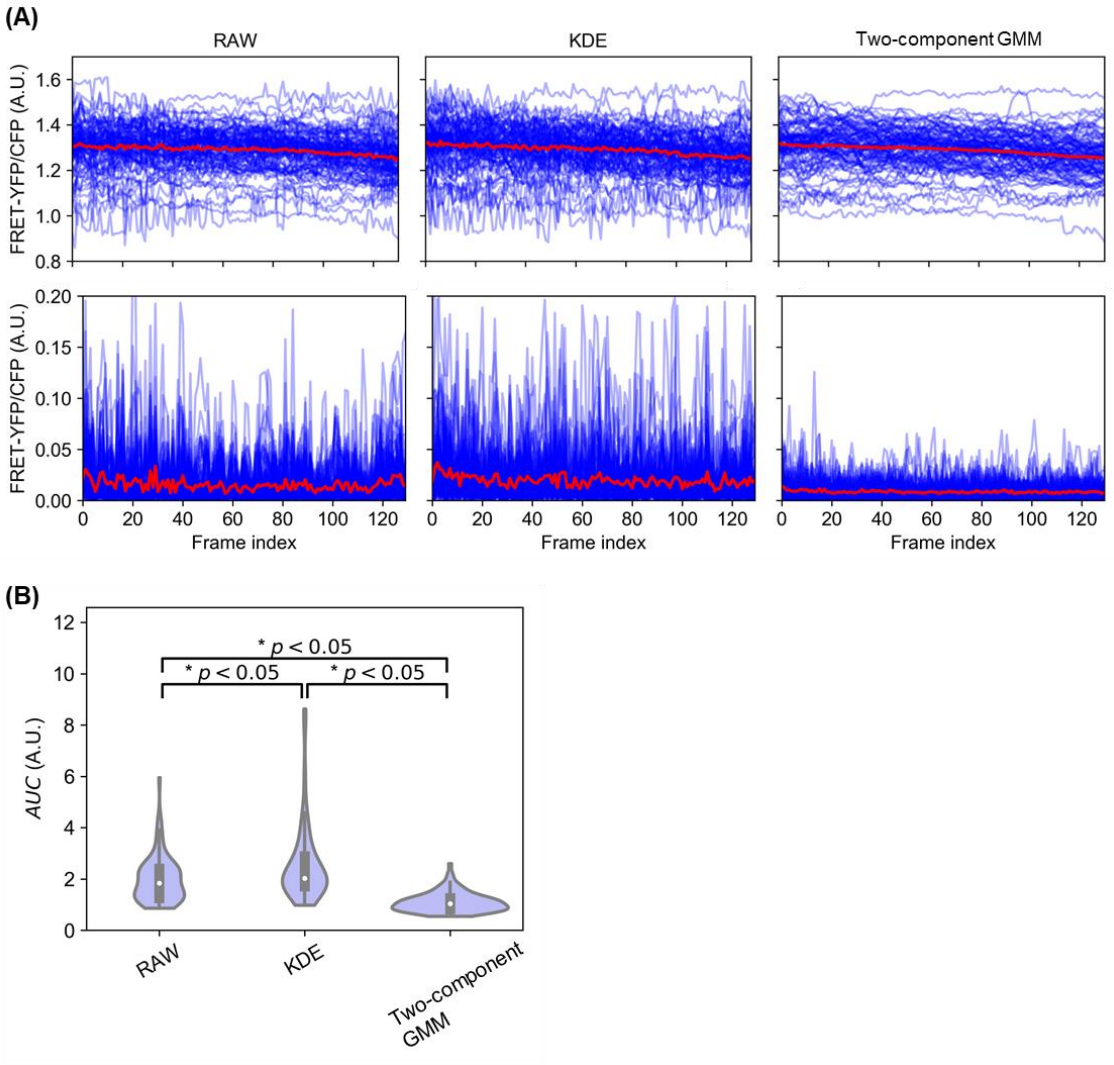

Fig. 10 Comparison of accuracy of background corrections using RAW, KDE and two-component GMM. (A) Upper panels: time series of the FRET-ratio (FRET-YFP/CFP) of individual myotubes in RAW, KDE, and GMM, respectively (n = 96, eight stage positions). Here, we used the same time lapse fluorescence images for all background corrections using RAW, KDE, and two-component GMM. One blue line corresponds to the time series of one myotube. The red line indicates the average time series of FRET ratio of myotubes in each background correction. Lower panels: absolute first-order difference of the time-series of the FRET ratio of individual myotubes in

each background correction. The red line indicates the mean time series of the absolute first order differential time series. (B) *AUC* distributions of the absolute first order difference of the time-series of myotubes in each background correction. *, $p < 0.05$ (Steel-Dwass test). In each violin plot, box plots are shown in the inset, and a white dot denotes the median.

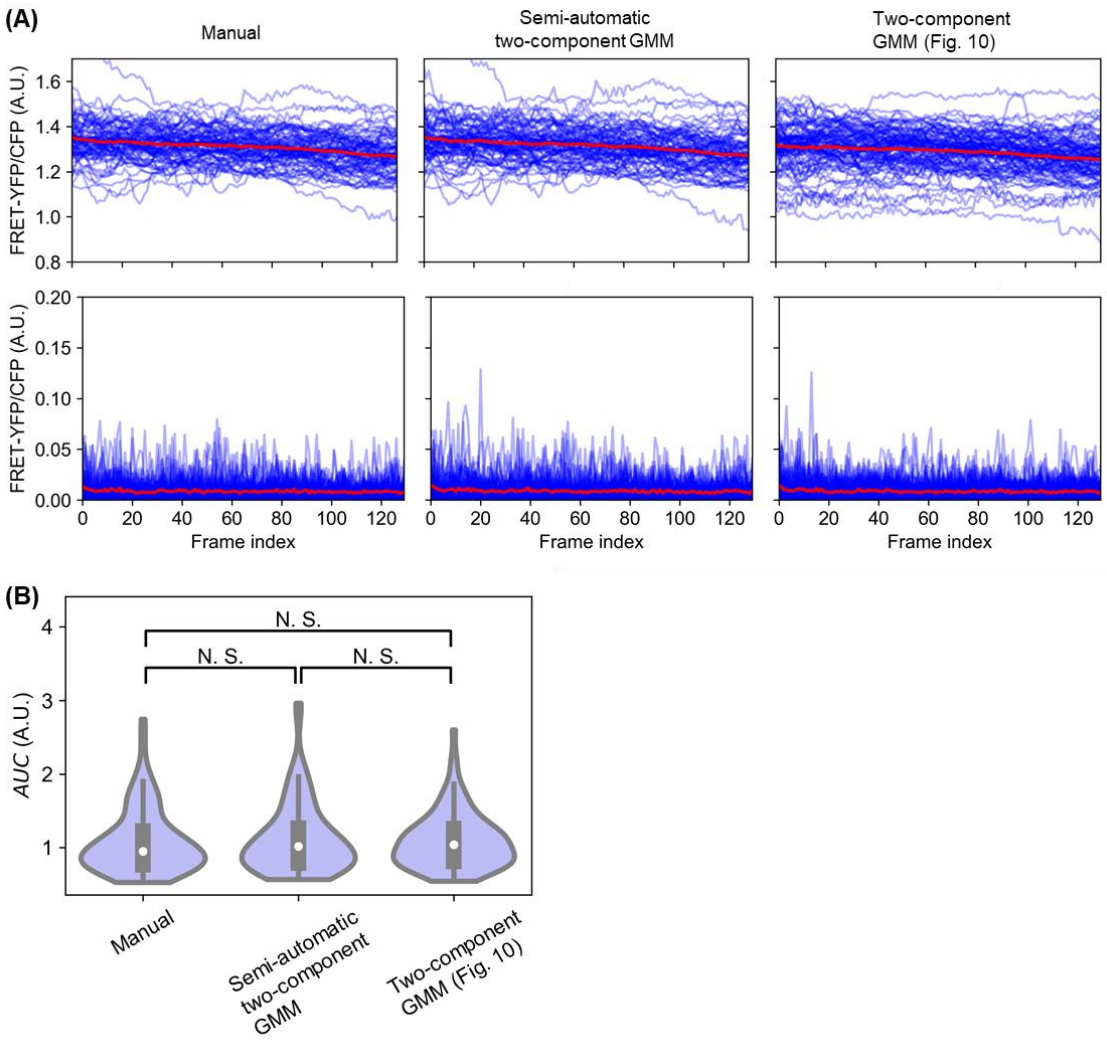

Fig. 11 Comparison of accuracy of background correction using Manual and semi-automatic two-component GMM. (A) Upper panels: time series of the FRET ratio (FRET-YFP/CFP) of individual myotubes in Manual and semi-automatic two-component GMM, respectively (n = 80, eight stage positions). The result of background correction using automatic myotube segmentation and two-component GMM in Fig. 10 was shown (two-component GMM). One blue line corresponds to the time series of one myotube. The red line indicates the average time series of the FRET ratio of myotubes in each background correction. Lower panels: absolute first order difference of time series

of the FRET ratio of individual myotubes in each background correction. The red line indicates the average time series of the absolute first order difference of the time series. (B) *AUC* distributions of the absolute first order difference of the time-series of myotubes in each background correction. N. S. (Not significant), $p > 0.05$ (Steel-Dwass test). In each violin plot, box plots are shown in the inset, and a white dot denotes the median.

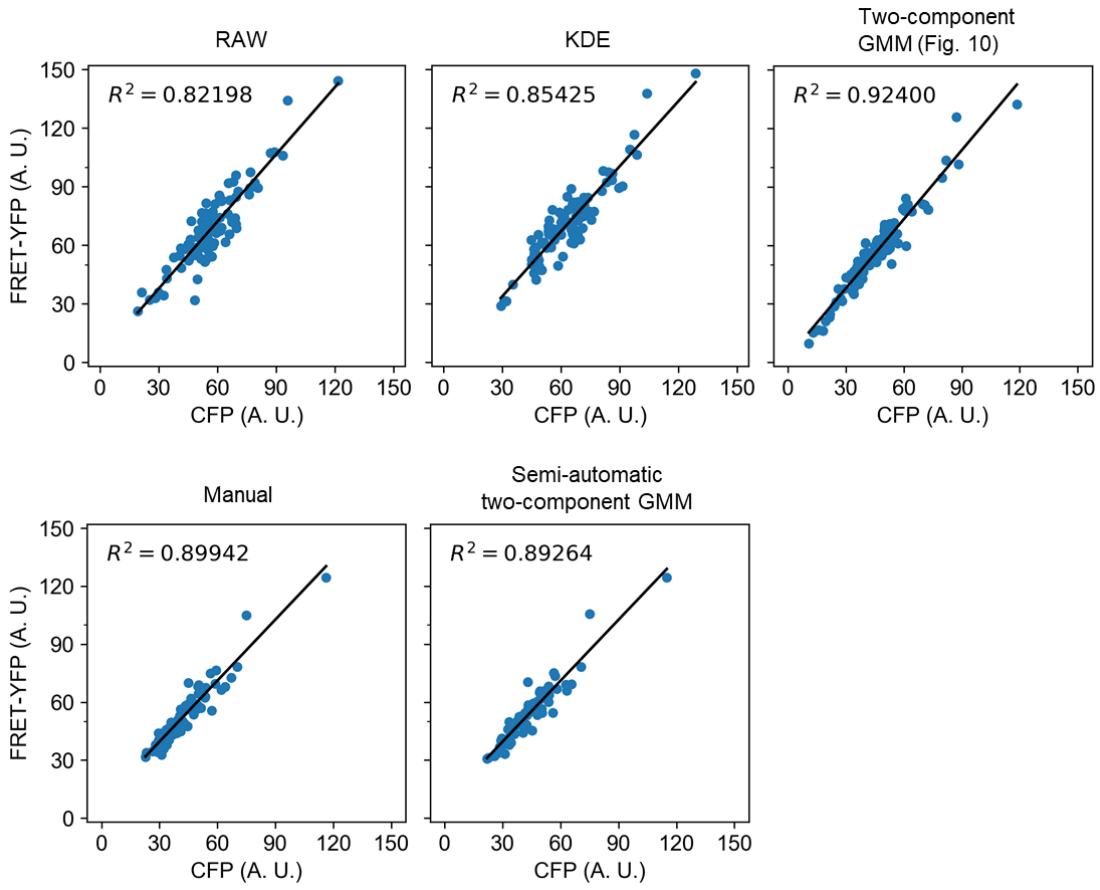

Fig. 12 Coefficients of determination of the *AUCs* in eq. (3) between CFP and FRET-YFP in each quantification method. One dot corresponds one myotube. The black line is the regression of the *AUC*s of CFP and FRET-YFP.

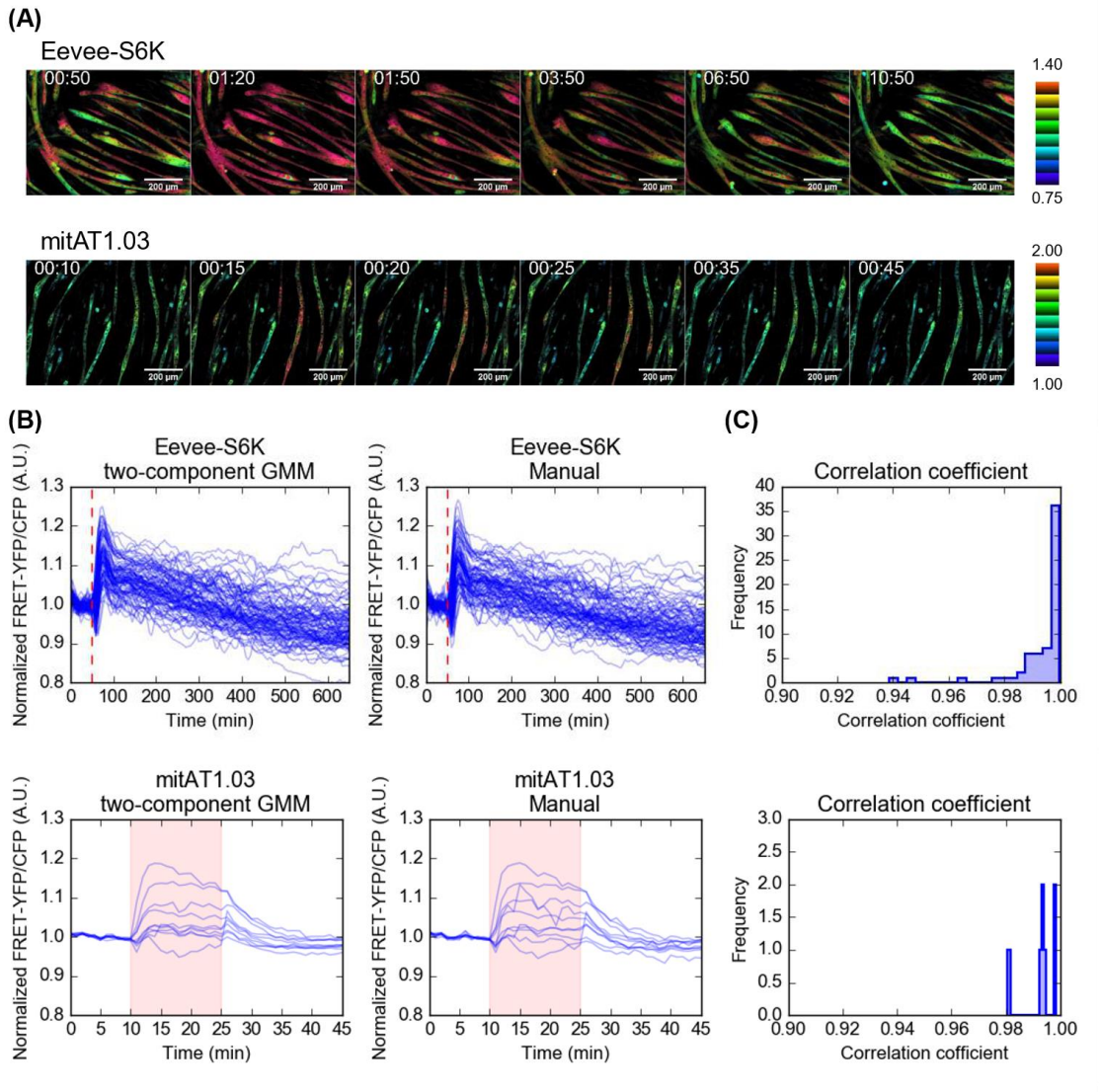

Fig. 13 Quantification of signal activity of S6K and ATP concentration by applying the developed method. (A) Time-lapse of the FRET ratio image. Differentiated C2C12 cells stably expressing Eevee-S6K were stimulated with 100 nM of insulin at 50 min. Differentiated C2C12 cells stably expressing mitAT1.03 were stimulated with EPS (10 ms with 50 V, 1Hz interval) at 10 min and continued for 15 min. (B) A time series of the FRET ratio (FRET-YFP/CFP) in response to insulin (n = 90, eight stage positions) and EPS (n = 10, one stage position) quantified by two-component GMM and quantified by

Manual (n = 80, eight stage positions, insulin; and n = 10, one stage position, EPS). One blue line corresponds one myotube. The red dashed line indicates time points of insulin stimulation. The red filled area indicates a period of EPS. (C) Histograms of Pearson's correlation coefficients of the time series of the FRET ratio between two-component GMM and Manual in response to insulin (Upper panels) and EPS (Lower panels).

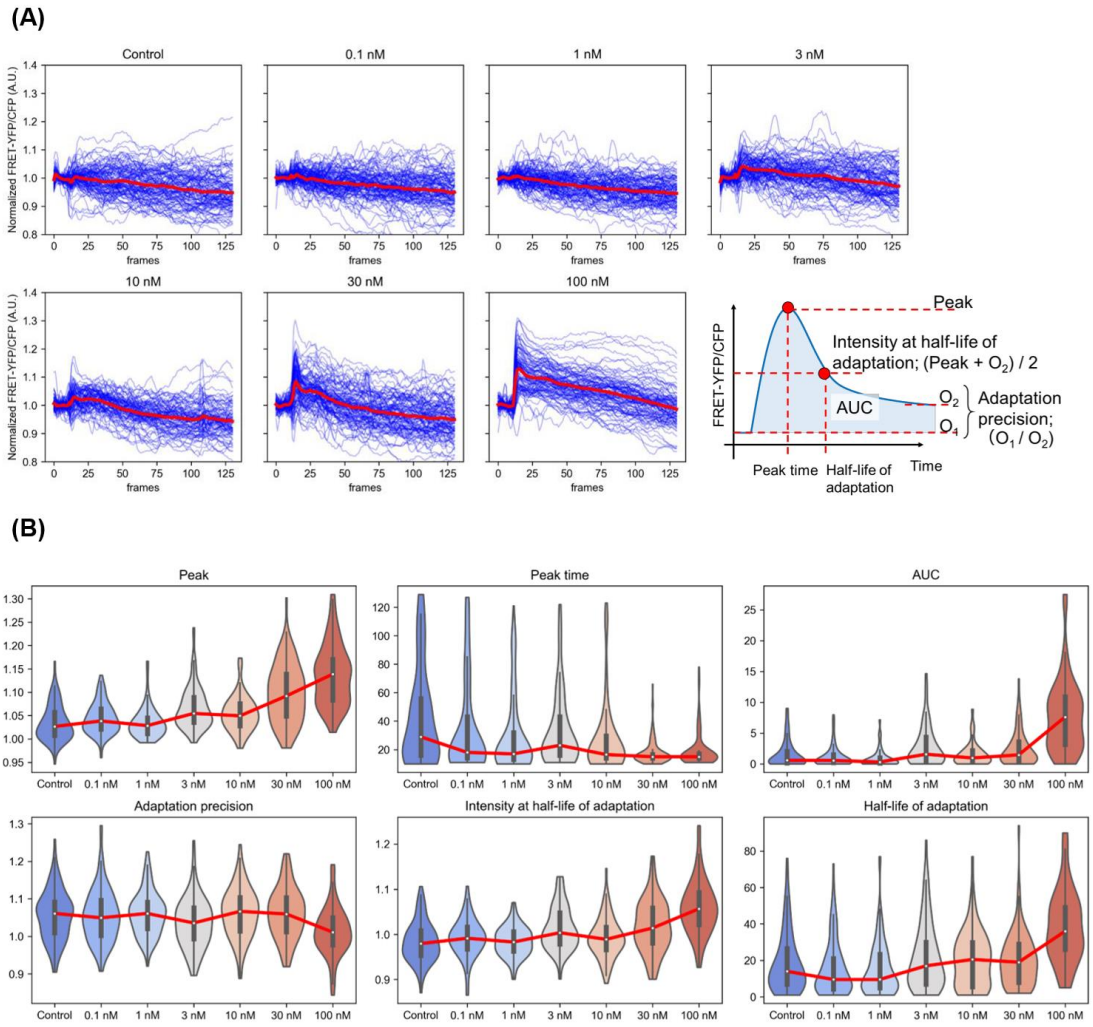

Fig. 14 Insulin-dependent S6K activation in individual myotubes and cell population. (A) Time series of the FRET ratio (FRET-YFP/CFP) in response to various doses of insulin in individual myotubes. From Control to 100 nM, number of myotubes were n = 98, 102, 100, 97, 86, 103 and 98, respectively. One blue line corresponds to the time series of one myotube. The red line indicates the average of each time series. Lower right panel is the definition of the characteristics of time series. (B) The cell population response of the time series in (A). In each violin plot, box plots are shown in the inset, and a white dot denotes the median. The red line indicates the average series of each character.

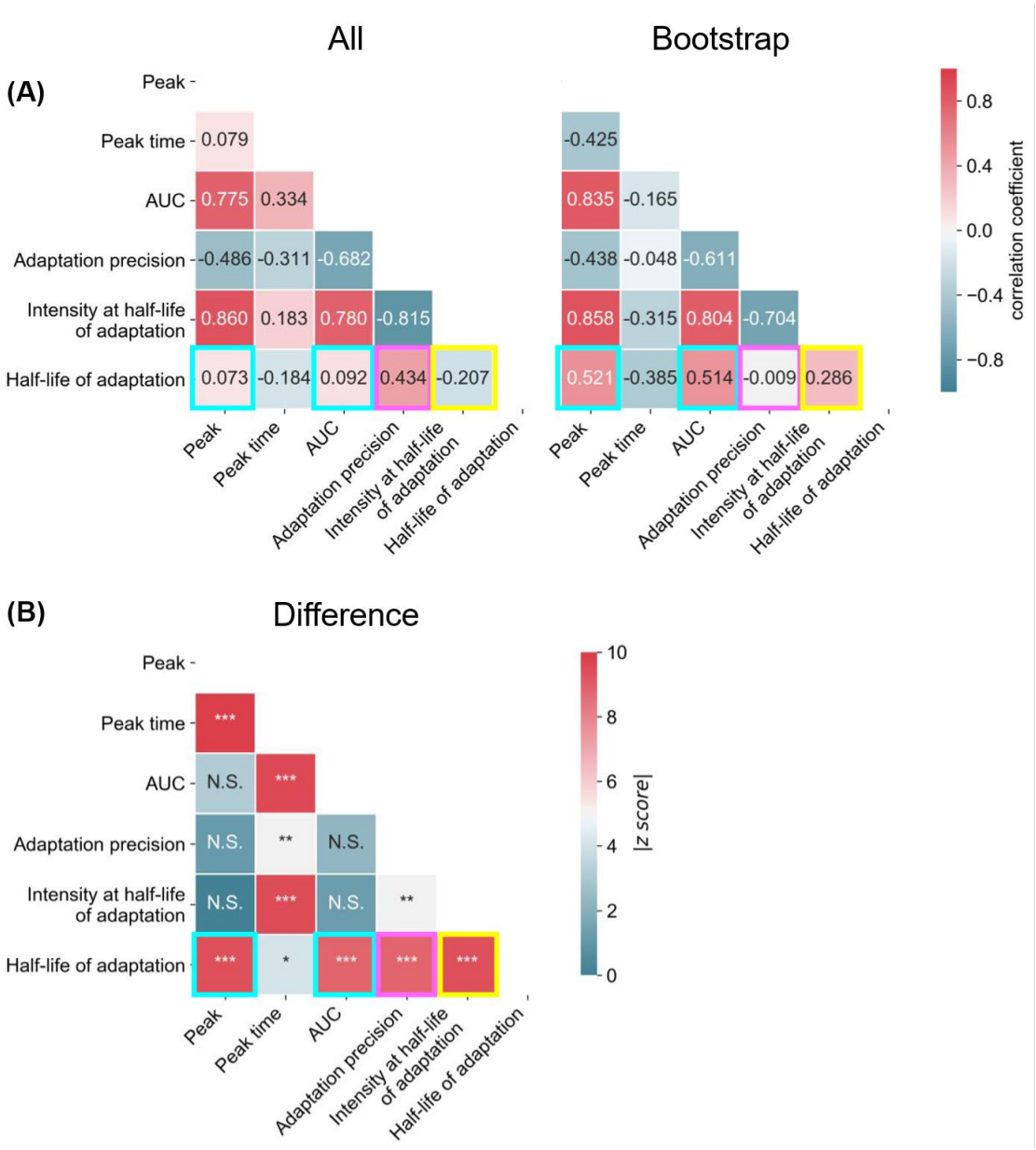

Fig. 15 Correlation between the characteristics in individual myotubes and population. (A) Spearman's rank correlation coefficients between the properties. All (n = 684) and Bootstrap (n = 700) indicate the correlations in all individuals and bootstrap subsets of population of myotubes, respectively. The bootstrap subsets in each dose data were generated by iterating 100 times to randomly sample 10 points and calculate the median. Cyan rectangles; the correlations higher in the

cell population than in the individuals, magenta rectangles; the correlation higher in the individuals than in the cell population, yellow rectangles; the reversed correlation between the cell population and individuals. (B) The difference in correlation coefficients between All and Bootstrap. N. S. (Not significant), $*p < 10^{-3}$, $**p < 10^{-5}$, $***p < 10^{-7}$. z score is a test static of the difference between two correlation coefficients (see Materials and methods).

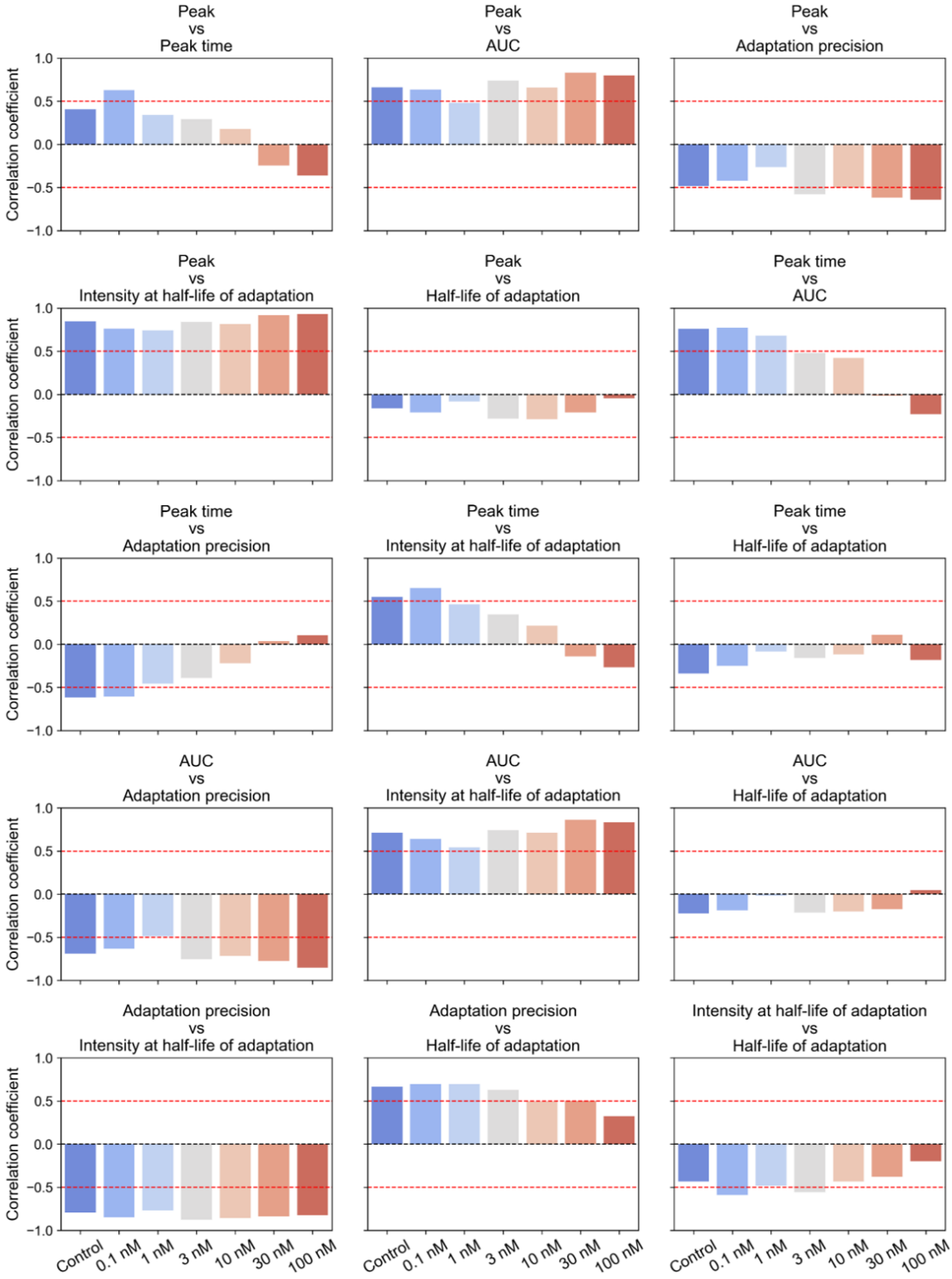

Fig. 16 Correlation coefficient between the characteristics in each dose of insulin in individuals

(All). The black and red dashed line indicates $|r| = 0$ and 0.5, respectively.

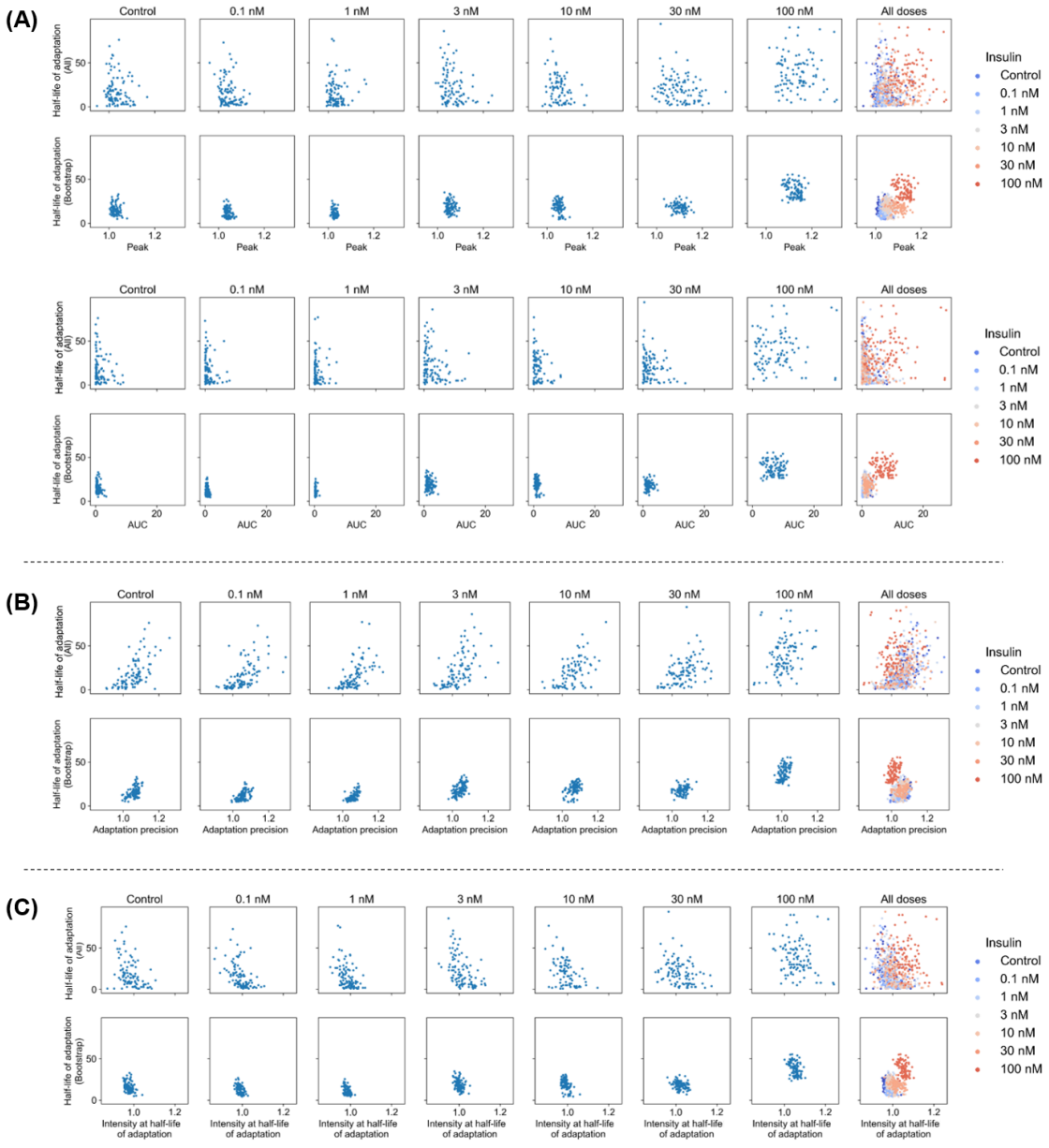

Fig. 17 Relationships between the characteristics in individual myotubes. (A) The characteristics showing the correlation higher in bootstrap subsets of population than in individuals. (B) The characteristics showing the correlation stronger in individuals than in bootstrap subsets of population. (B) The characteristics showing the reversed relationship in individuals and in bootstrap subsets of population.

Table 1 Parameters used for pre-processing.

Parameter	Value (pixel)	Description
median filter[a]	5	side length of filter window
white top hat[b]	35	side length of filter window
white top hat[c]	30	side length of filter window
threshold size[d]	10000	threshold area of myotube

(a) is the common value in detection of myotubes and detection of myotube centers. (b) is used for detection of myotubes. (c) is used for detection of myotube centers. (d) is used after watershed segmentation.

Table 2 Computation time.

Step	Mean ± S.D. (sec)	Max (sec)
Detection of myotubes (Step II-i to II-iii)[a]	6.13 ± 0.52	6.82
Detection of myotube centers (Step II-iv to II-x)[b]	24.97 ± 3.72	32.33
Watershed (Step II-xi)[c]	-	-
Background correction (Step III)[d]	2.94 ± 0.84	4.73

Because (a), (b) and (c) are batch processes, the computation times were measured for each dataset (1344×1024 pixels, 131 frames) with eight stage positions (n = 8). (c) was too fast to measure the computation time. Because of (d) is a sequential process for each image, the computation time was measured in each image (131 frames, eight stage positions, n = 1048).

Data Availability

The datasets of time-lapse images, segmentation results and segmentation programs are available from our database (http://kurodalab.org/info/Inoue).

Acknowledgements

I would like to thank Professor Shinya Kuroda for giving me critical direction to write this paper. I thank Dr. Katsuyuki Kunida for his advices on treatments of cells and microscopy. I thank Dr. Daisuke Hoshino for his insightful advice about muscle cells. I thank Dr. Shinsuke Uda for helpful discussions and technical advice for image analysis. I thank Dr. Masashi Fuji and Dr. Atsushi Hatano for their critical reading of this paper, helpful discussions, and technical advice with experiments. I thank Mr. Takumi Wada and Mr. Naoki Matsuda for their everyday discussion and helping with experiments. I am also grateful to Dr. Kazuhiro Aoki (National Institute for Basic Biology), Dr. Hiromi Imamura (Kyoto University) and Dr. Hiroyuki Noji (University of Tokyo) for kindly providing FRET biosensors, Eevee-S6K and mitAT1.03. I would like to express appreciation to all the members of Kuroda laboratory for giving me a fulfilling research life.

This work was supported by the Creation of Fundamental Technologies for Understanding and Control of Biosystem Dynamics, CREST, of the Japan Science and Technology Agency (JST)(#JPMJCR12W3) and by the Japan Society for the Promotion of Science (JSPS) KAKENHI

Grant Number (17H06300, 17H06299, 18H03979). Katsuyuki Kunida receives funding from a Grant-in-Aid for Young Scientists (B) (#16K19028).

References

[1] B. Alberts *et al.*, Eds., *Molecular Biology of the Cell*, 6th ed. New York and Abingdon: Garland Science, 2014.

[2] R. Lev Bar-Or, R. Maya, L. A. Segel, U. Alon, A. J. Levine, and M. Oren, "Generation of oscillations by the p53-Mdm2 feedback loop: A theoretical and experimental study," *Proc. Natl. Acad. Sci.*, 2000.

[3] R. Cheong, A. Bergmann, S. L. Werner, J. Regal, A. Hoffmann, and A. Levchenko, "Transient IκB Kinase Activity Mediates Temporal NF-κB Dynamics in Response to a Wide Range of Tumor Necrosis Factor-α Doses," *J. Biol. Chem.*, vol. 281, no. 5, pp. 2945–2950, Feb. 2006.

[4] J. E. Ferrell and E. M. Machleder, "The biochemical basis of an all-or-none cell fate switch in Xenopus oocytes.," *Science*, vol. 280, no. 5365, pp. 895–8, May 1998.

[5] G. Lahav *et al.*, "Dynamics of the p53-Mdm2 feedback loop in individual cells," *Nat. Genet.*, vol. 36, no. 2, pp. 147–150, Feb. 2004.

[6] J. E. Purvis and G. Lahav, "Encoding and Decoding Cellular Information through Signaling Dynamics," *Cell*, vol. 152, no. 5, pp. 945–956, Feb. 2013.

[7] S. Tay, J. J. Hughey, T. K. Lee, T. Lipniacki, S. R. Quake, and M. W. Covert, "Single-cell NF-κB dynamics reveal digital activation and analogue information processing," *Nature*, vol. 466, no. 7303, pp. 267–271, Jul. 2010.

[8] R. Cheong, A. Rhee, C. J. Wang, I. Nemenman, and A. Levchenko, “Information Transduction Capacity of Noisy Biochemical Signaling Networks,” *Science (80-.).*, vol. 334, no. 6054, pp. 354–358, Oct. 2011.

[9] T. Meyer and M. N. Teruel, “Fluorescence imaging of signaling networks,” *Trends Cell Biol.*, vol. 13, no. 2, pp. 101–106, Feb. 2003.

[10] J. Lippincott-Schwartz, E. Snapp, and A. Kenworthy, “Studying protein dynamics in living cells,” *Nat. Rev. Mol. Cell Biol.*, vol. 2, no. 6, pp. 444–456, Jun. 2001.

[11] P. Bajcsy *et al.*, “Survey statistics of automated segmentations applied to optical imaging of mammalian cells,” *BMC Bioinformatics*, vol. 16, no. 1, p. 330, 2015.

[12] M. Kodiha, P. Bański, and U. Stochaj, “Computer-based fluorescence quantification: a novel approach to study nucleolar biology.,” *BMC Cell Biol.*, vol. 12, no. June, p. 25, 2011.

[13] J. CHALFOUN *et al.*, “Segmenting time-lapse phase contrast images of adjacent NIH 3T3 cells,” *J. Microsc.*, vol. 249, no. 1, pp. 41–52, Jan. 2013.

[14] J. Chalfoun, M. Majurski, A. Dima, C. Stuelten, A. Peskin, and M. Brady, “FogBank: a single cell segmentation across multiple cell lines and image modalities.,” *BMC Bioinformatics*, vol. 15, no. 1, p. 6598, 2014.

[15] E. Hodneland, X. C. Tai, and H. Kalisch, “PDE Based Algorithms for Smooth Watersheds,” *IEEE Trans. Med. Imaging*, vol. 35, no. 4, pp. 957–966, 2016.

[16] L. C. Wong, B. Lu, K. W. Tan, and M. Fivaz, “Fully-automated image processing software to analyze calcium traces in populations of single cells,” *Cell Calcium*, vol. 48, no. 5, pp. 270–274, 2010.

[17] J. Fodor, A. Gomba-Tóth, T. Oláh, J. Almássy, E. Zádor, and L. Csernoch, “Follistatin treatment suppresses SERCA1b levels independently of other players of calcium homeostasis in C2C12 myotubes,” *J. Muscle Res. Cell Motil.*, vol. 38, no. 2, pp. 215–229, Apr. 2017.

[18] B. Rahar, S. Chawla, S. Pandey, A. N. Bhatt, and S. Saxena, “Sphingosine-1-phosphate pretreatment amends hypoxia-induced metabolic dysfunction and impairment of myogenic potential in differentiating C2C12 myoblasts by stimulating viability, calcium homeostasis and energy generation,” *J. Physiol. Sci.*, vol. 68, no. 2, pp. 137–151, Mar. 2018.

[19] E. Rapizzi, C. Donati, F. Cencetti, P. Nincheri, and P. Bruni, “Sphingosine 1-phosphate differentially regulates proliferation of C2C12 reserve cells and myoblasts,” *Mol. Cell. Biochem.*, vol. 314, no. 1–2, pp. 193–199, 2008.

[20] Q. A. Soltow, E. H. Zeanah, V. A. Lira, and D. S. Criswell, “Cessation of cyclic stretch induces atrophy of C2C12 myotubes,” *Biochem. Biophys. Res. Commun.*, vol. 434, no. 2, pp. 316–321, 2013.

[21] N. Yoshida, S. Yoshida, K. Koishi, K. Masuda, and Y. Nabeshima, “Cell heterogeneity upon myogenic differentiation: down-regulation of MyoD and Myf-5 generates ‘reserve cells’.,” *J. Cell*

Sci., vol. 111 (Pt 6, pp. 769–79, Mar. 1998.

[22] M. Laplante and D. M. Sabatini, "MTOR signaling in growth control and disease," *Cell*, vol. 149, no. 2, pp. 274–293, 2012.

[23] C. C. Dibble and L. C. Cantley, "Regulation of mTORC1 by PI3K signaling.," *Trends Cell Biol.*, vol. 25, no. 9, pp. 545–55, Sep. 2015.

[24] A. González and M. N. Hall, "Nutrient sensing and TOR signaling in yeast and mammals.," *EMBO J.*, vol. 36, no. 4, pp. 397–408, Feb. 2017.

[25] L. R. Pearce, D. Komander, and D. R. Alessi, "The nuts and bolts of AGC protein kinases," *Nat. Rev. Mol. Cell Biol.*, vol. 11, no. 1, pp. 9–22, 2010.

[26] L. Khamzina, A. Veilleux, S. Bergeron, and A. Marette, "Increased Activation of the Mammalian Target of Rapamycin Pathway in Liver and Skeletal Muscle of Obese Rats: Possible Involvement in Obesity-Linked Insulin Resistance," *Endocrinology*, vol. 146, no. 3, pp. 1473–1481, Mar. 2005.

[27] K. Aoki and M. Matsuda, "Visualization of small GTPase activity with fluorescence resonance energy transfer-based biosensors.," *Nat. Protoc.*, vol. 4, no. 11, pp. 1623–1631, 2009.

[28] F. Leymarie and M. D. Levine, "Fast raster scan distance propagation on the discrete rectangular lattice," *CVGIP Image Underst.*, vol. 55, no. 1, pp. 84–94, Jan. 1992.

[29] N. Otsu, "A Threshold Selection Method from Gray-Level Histograms," *IEEE Trans. Syst. Man.*

Cybern., vol. 9, no. 1, pp. 62–66, Jan. 1979.

[30] G. W. Zack, W. E. Rogers, and S. A. Latt, “Automatic measurement of sister chromatid exchange frequency.,” *J. Histochem. Cytochem.*, vol. 25, no. 7, pp. 741–753, Jul. 1977.

[31] M. LEVANDOWSKY and D. WINTER, “Distance between Sets,” *Nature*, vol. 234, no. 5323, pp. 34–35, Nov. 1971.

[32] T. Zimmermann, J. Rietdorf, and R. Pepperkok, “Spectral imaging and its applications in live cell microscopy,” *FEBS Lett.*, vol. 546, no. 1, pp. 87–92, 2003.

[33] K. K. Ceelen, C. W. J. Oomens, a. Stekelenburg, D. L. Bader, and F. P. T. Baaijens, “Changes in Intracellular Calcium during Compression of C2C12 Myotubes,” *Exp. Mech.*, vol. 49, no. 1, pp. 25–33, 2007.

[34] M. Horie, E. Warabi, S. Komine, S. Oh, and J. Shoda, “Cytoprotective role of Nrf2 in electrical pulse stimulated C2C12 myotube,” *PLoS One*, vol. 10, no. 12, pp. 1–13, 2015.

[35] H. Imamura *et al.*, “Visualization of ATP levels inside single living cells with fluorescence resonance energy transfer-based genetically encoded indicators,” *Proc Natl Acad Sci U S A*, vol. 106, no. 37, pp. 15651–15656, 2009.

[36] S. J. Odelberg, A. Kollhoff, and M. T. Keating, “Dedifferentation of mammalian myotubes induced by msx1,” *Cell*, vol. 103, no. 7, pp. 1099–1109, 2000.

[37] N. Komatsu *et al.*, “Development of an optimized backbone of FRET biosensors for kinases and

GTPases.," *Mol. Biol. Cell*, vol. 22, no. 23, pp. 4647–56, Dec. 2011.

[38] T. Huang, G. Yang, and G. Tang, "A fast two-dimensional median filtering algorithm," *IEEE Trans. Acoust.*, vol. 27, no. 1, pp. 13–18, Feb. 1979.

[39] L. Coelho, "Mahotas: Open source software for scriptable computer vision," *J. Open Res. Softw.*, vol. 1, no. 1, p. e3, Jul. 2013.

[40] S. van der Walt *et al.*, "scikit-image: image processing in Python," *PeerJ*, vol. 2, p. e453, Jun. 2014.

[41] F. Pedregosa *et al.*, "Scikit-learn: Machine Learning in Python," *J. Mach. Learn. Res.*, vol. 12, pp. 2825–2830, Jan. 2011.

[42] J. Schindelin *et al.*, "Fiji: an open-source platform for biological-image analysis.," *Nat. Methods*, vol. 9, no. 7, pp. 676–82, Jun. 2012.

[43] A. A. Dima *et al.*, "Comparison of segmentation algorithms for fluorescence microscopy images of cells," *Cytom. Part A*, vol. 79A, no. 7, pp. 545–559, Jul. 2011.

[44] D. A. Van Valen *et al.*, "Deep Learning Automates the Quantitative Analysis of Individual Cells in Live-Cell Imaging Experiments," *PLOS Comput. Biol.*, vol. 12, no. 11, p. e1005177, Nov. 2016.

[45] S. Uda *et al.*, "Robustness and compensation of information transmission of signaling pathways.," *Science*, vol. 341, no. 6145, pp. 558–61, Aug. 2013.

[46] J. Selimkhanov *et al.*, "Accurate information transmission through dynamic biochemical signaling networks," *Science (80-.).*, vol. 346, no. 6215, pp. 1370–1373, Dec. 2014.

[47] S. Krishnaswamy *et al.*, “Conditional density-based analysis of T cell signaling in single-cell data,” *Science (80-.).*, vol. 346, no. 6213, pp. 1250689–1250689, Nov. 2014.

[48] M. D. Brennan, R. Cheong, and A. Levchenko, “How Information Theory Handles Cell Signaling and Uncertainty,” *Science (80-.).*, vol. 338, no. 6105, pp. 334–335, Oct. 2012.

[49] A. Levchenko and I. Nemenman, “Cellular noise and information transmission,” *Curr. Opin. Biotechnol.*, vol. 28, pp. 156–164, Aug. 2014.

[50] D. W. D. West *et al.*, “Acute resistance exercise activates rapamycin-sensitive and -insensitive mechanisms that control translational activity and capacity in skeletal muscle.,” *J. Physiol.*, vol. 594, no. 2, pp. 453–68, Jan. 2016.

[51] K. Baar and K. Esser, “Phosphorylation of p70(S6k) correlates with increased skeletal muscle mass following resistance exercise.,” *Am. J. Physiol.*, vol. 276, no. 1 Pt 1, pp. C120-7, Jan. 1999.

[52] L. Deldicque *et al.*, “Antagonistic effects of leucine and glutamine on the mTOR pathway in myogenic C2C12 cells.,” *Amino Acids*, vol. 35, no. 1, pp. 147–55, Jun. 2008.

[53] J. L. Areta, J. A. Hawley, J.-M. Ye, M. H. S. Chan, and V. G. Coffey, “Increasing leucine concentration stimulates mechanistic target of rapamycin signaling and cell growth in C2C12 skeletal muscle cells,” *Nutr. Res.*, vol. 34, no. 11, pp. 1000–1007, 2014.

[54] P. Dalle Pezze *et al.*, “A systems study reveals concurrent activation of AMPK and mTOR by amino acids.,” *Nat. Commun.*, vol. 7, p. 13254, 2016.